J. Fluid Mech. (1996), *vol.* 323, *pp.* 201–236

Singular effects of surface tension in evolving Hele-Shaw flows

By MICHAEL SIEGEL[1], SALEH TANVEER[2] AND WEI-SHEN DAI[3]

[1] Mathematics Department, New Jersey Institute of Technology, Newark, NJ 07102, USA

[2] Mathematics Department, Ohio State University, Columbus, OH 43210, USA

[3] Electrotechnical Laboratory, Supermolecular Section, Tsubcuba, Ibaraki 305, Japan

(Received 25 June 1995 and in revised form 9 February 1996)

In this paper, we present evidence to show that a smoothly evolving zero-surface tension solution of the Hele-Shaw equations can be singularly perturbed by the presence of arbitrarily small non-zero surface tension in order-one time. These effects are explained by the impact of 'daughter singularities' on the physical interface, whose formation was suggested in a prior paper (Tanveer 1993). For the case of finger motion in a channel, it is seen that the daughter singularity effect is strong enough to produce the transition from a finger of arbitrary width to one with the selected steady-state width in $O(1)$ time.

1. Introduction

The penetration of a gas into a viscous fluid in a Hele-Shaw cell is the simplest member of a class of related pattern formation problems that include dendritic crystal growth, directional solidification, and electro-deposition. For Hele-Shaw flow in a channel, a steadily advancing flat interface is unstable to perturbations when driven by the gas. The perturbations grow into fingers which then exhibit several interesting features; these include side-branching and fingertip splitting, followed by multiple finger formation and competition. Recently there has been much progress in understanding the structure and linear stability of steady finger solutions in the presence of surface tension. Some of the newer developments in this area are reviewed by Pelce (1988), Kessler, Koplik & Levine (1988), Howison (1991), and Tanveer (1991) from a range of different perspectives. Earlier work is summarized by Saffman (1986), Bensimon *et al.* (1986), and Homsy (1987).

Most of the work in the initial value problem for non-zero surface tension has been numerical in nature. For channel flow, DeGregoria & Schwartz (1985, 1986) find that a finger of air propagating into the fluid spontaneously splits when surface tension is sufficiently small. Bensimon (1986) and Dai & Shelley (1994) show that there is great sensitivity to the level of precision in numerical calculations for small values of the surface tension coefficient. Their results provide numerical evidence supporting arguments (Bensimon 1986) that the size of the perturbation triggering the tip-splitting instability decreases quickly with decreasing surface tension. Other numerical studies are given by Tryggvason & Aref (1983, 1985) and Meiburg & Homsy (1988). Experimental observations show that, in the limit of small capillary

effects, even noise can be large enough to set off a pattern of continual tip-splitting and finger competition (Maxworthy 1987; Arneodo *et al.* 1989).

The numerical methods produce results qualitatively similar to experimental results. In particular, for small enough surface tension the sensitivity to the level of 'noise' produces a random pattern of fingers undergoing tip-splitting followed by competition. Despite this unpredictability, Arneodo *et al.* (1989) observe a remarkable connection between *statistical* properties of the highly irregular time-dependent pattern and the steady-state finger. Unfortunately, numerical work has yet to provide a clear understanding of such phenomena or of the asymptotic trends in the limit as surface tension tends to zero. Ideally, one would like to be able to theoretically predict the scaling dependence of the complicated interfacial pattern on the surface tension parameter.

Analytical work for non-zero surface tension is scarce; a local existence result has been obtained by Duchon & Robert (1984), and a global in time result (for flow in a radial geometry with small initial perturbations) by Constantin & Pugh (1993). When surface tension is exactly zero, the mathematical problem simplifies to a great degree because of the absence of the curvature term. There has been quite a bit of analytical work in this case. Exact solutions and solution methods were discovered by researchers in Russia (Galin 1945; Polubarinova-Kochina 1945) for a class of initial conditions. Without knowledge of these methods, other solutions were found that can be seen to follow from their general procedure (see for instance Saffman; 1959, Howison 1985, 1986*a*, *b*; Richardson 1972; Shraiman & Bensimon 1985). The class of known exact solutions has been used by Howison (1986) to demonstrate the ill-posedness of the initial value problem for the interface; it is possible to choose two initial conditions which are arbitrarily close in any Sobolev norm (defined on the physical interface), yet which differ by $O(1)$ over a time which can be made arbitrarily small.

These theoretical results are often described in terms of a conformal map $z(\zeta, t)$ that takes the interior of a unit circle in the ζ-plane to the physical flow domain; the unit circle itself is mapped to the free surface. The conformal map must be analytic inside the unit disk, aside from a fixed singularity at $\zeta = 0$ (required due to the infinite extent of the fluid region), but it may have singularities and zeros outside it. These can move toward the boundary of the unit disk and reach it in finite time, at which point a singularity appears on the interface. The origin of ill-posedness, then, is that small perturbations on the interface can introduce a zero or a singularity in z_ζ outside the unit disk, which subsequently impinges on it quickly. Following the work of Richardson (1972) and Lacey (1982), Tanveer (1993) showed that all singularities will move towards the unit disk, while preserving their type.

The ill-posedness of the zero-surface-tension problem makes it difficult to understand the effect of small non-zero surface tension. A perturbative study of the interfacial motion is accompanied by severe mathematical difficulties. If $\mathscr{S}_0(t)$ is the solution operator that maps an initial condition into the zero-surface-tension solution at a time t, then the ill-posedness of the zero surface tension problem implies that $\mathscr{S}_0$ is unbounded with respect to any norm defined on the physical interface. Thus there is no a *priori* reason to expect that the solution operator $\mathscr{S}(t)$ for non-zero surface tension will approach $\mathscr{S}_0(t)$ in the small surface tension limit.

Recently, one of us (Tanveer 1993) has suggested a way to avoid these mathematical difficulties by imbedding the zero-surface-tension problem in a well-posed problem. This can be done by analytically extending the initial value problem for $z(\zeta, t)$ into the region exterior to the unit disk. When data are specified in $|\zeta| > 1$ (say, with

$z(\zeta,0)$ given in closed form) the initial value problem is well-posed, and the interface evolves without sensitivity to initial conditions. This extension is the basis of a recent (Baker, Siegel & Tanveer 1995) numerical method through which solution of the zero-surface-tension initial value problem can be computed in a well-posed manner.

Here, we consider the effect of small non-zero surface tension on the evolution of initial data $z(\zeta,0)$ specified in the extended complex plane. The well-posed formulation of the zero-surface-tension problem allows the effects of small surface tension on prescribed initial data in $|\zeta| \geqslant 1$ to be treated perturbatively. More precisely, in the extended domain one can consider a perturbation expansion of the form

$$z \sim z_0 + Bz_1 + \cdots \tag{1}$$

where B is an appropriate dimensionless surface tension parameter. It turns out that, for *early* times, surface tension is a regular perturbation except in the neighbourhood of initial zeros and certain singularities of z_ζ. Tanveer (1993) has performed an asymptotic study of the effect of small surface tension on initial zeros of z_ζ as well as on isolated singularities in the initial data of the form

$$z_\zeta(\zeta,0) \sim A(0)(\zeta - \zeta_s(0))^{-\beta}, \quad \beta > 0 \tag{2}$$

for $|\zeta_s(0)| > 1$. Interestingly, it is found that initial singularities with β in the interval (0, 4/3) and initial zeros are transformed into clusters of $-4/3$ singularities. In contrast, when $B = 0$ the singularities and zeros preserve their form. All singularities approach the physical domain $|\zeta| = 1$, and many of them eventually create large deformations of the interface.

One of the most interesting phenomena predicted in the asymptotic study is the presence of singularities of z at points in the extended domain where $z_0(\zeta,t)$, the corresponding zero-surface-tension solution, is a perfectly well-behaved function. These singularities are formed in clusters which remain intact until they come very close to the physical domain $|\zeta| = 1$. Each cluster is centred at a point, denoted by $\zeta_d(t)$ and referred to as a 'daughter singularity', where the regular perturbation expansion (1) breaks down, even though $z_{0\zeta}(\zeta_d,t)$ is neither singular nor zero. Based on some assumptions, it was shown that there is an $O(B^{1/3})$ sized region around each point $\zeta_d(t)$ where surface tension effects play a singular role. In particular, z_ζ deviates from $z_{0\zeta}$ by $O(1)$ in this region. Each daughter singularity initially coincides with a zero of $z_{0\zeta}$; nonetheless, at later times the daughter singularity and zero move apart. As with all singularities, the daughter singularities move toward the physical domain $|\zeta| = 1$. This raises the interesting possibility that significant differences between the $B = 0$ and $0 < B \ll 1$ interfacial shapes could occur even when no zeros or singularities of $z_{0\zeta}$ are near $|\zeta| = 1$.

Unfortunately, the previous asymptotic results are restricted to times for which $|\zeta_d| - 1 \gg B^{1/3}$, when the daughter singularity is still too far from $|\zeta| = 1$ to have a noticeable effect on the interface. In this paper, we address the influence of daughter singularities beyond this stage, when their effects are actually felt on the physical interface. Our study is by two complementary approaches: an asymptotic theory which is an extension of Tanveer's results to the time when $|\zeta_d(t)| - 1 = O(B^{1/3})$, and a set of numerical solutions for the full equations. The numerics enable us to directly observe the consequences of the daughter singularities as they approach the physical domain, and to corroborate many of the analytically predicted scalings. This numerical confirmation is particularly important, since the asymptotics rely on several assumptions about the nature of the complex domain solution that are yet to be verified directly.

Our results show that arbitrarily small surface tension can be important over $O(1)$ times, even when the curvature predicted by the zero-surface-tension solution is not large. From a physical standpoint, this conclusion may appear surprising, since the magnitude of the surface tension term in the equations of motion is proportional to the curvature. However, there is a danger in attaching physical intuition to the zero-surface-tension problem owing to its ill-posedness in the physical domain. In fact, the actual curvature need not be close to that predicted by the corresponding zero-surface-tension solution, even when such solutions are smooth.

The daughter singularities do not always influence the physical interface in $O(1)$ time. Their effects are sometimes shielded or deferred by the presence of other singularities. In a general way, we develop an understanding of when and where daughter singularity effects will be felt on the physical interface by considering a number of different initial conditions for the radial as well as channel geometries. A preliminary report on our results for the channel geometry appears in Siegel & Tanveer (1996); this paper presents much more comprehensive analytical and numerical results, for both the radial and channel geometries.

This paper is arranged as follows. In §2, we present the governing equations for Hele-Shaw flow. We also discuss the formation of daughter singularities by examining the breakdown of a regular perturbation expansion in B near a zero of z_ζ. For concreteness, in §3 we present several exact zero-surface-tension solutions containing zeros of z_ζ. These will be used as initial data in simulations for non-zero B, performed in a later section. Inner equations valid in a neighbourhood of $\zeta_d(t)$ are summarized in §4. These equations are extended to the time when daughter singularity effects are felt on the physical domain. In §5, we present numerical simulations of Hele-Shaw evolution for a set of decreasing B. The calculations are reconciled with the analytically predicted scalings.

2. Governing equations

In this section we present the equations which govern interfacial flow in a Hele-Shaw cell, and examine their analytic continuation in the complex plane. We will follow closely the formulation of Tanveer (1993). We also consider a regular perturbation expansion in the surface tension parameter B, and discuss the points where this expansion breaks down. It is in a neighbourhood of these points where the singular effects of surface tension initially occur.

Consider first Hele-Shaw flow in a radial geometry (figure 1*a*), in which air of negligible viscosity displaces a viscous incompressible liquid. Introduce the conformal map $z(\zeta,t)$ which takes the interior of a unit circle in the ζ-plane into the viscous fluid region of the z-plane ($z = x + \mathrm{i}y$), such that $\zeta = 0$ is mapped to infinity. This map can be decomposed as

$$z(\zeta,t) = \frac{a(t)}{\zeta} + f(\zeta,t). \tag{3}$$

Inside the unit circle, $f(\zeta,t)$ must be analytic and $z_\zeta \neq 0$. For analytic boundary shapes, as assumed here, these conditions hold in an open set which contains the unit disk. We also require $a(t)$ to be real and positive. This is always possible in view of the remaining degree of freedom allowed by the Riemann mapping theorem.

For flow in the channel geometry, we analogously define a conformal map from the unit semicircle in the ζ-plane figure to the fluid region of the z-plane (figure 1*b*). The circular arc $|\zeta| = 1$ is mapped to the interface, and the diameter is mapped to

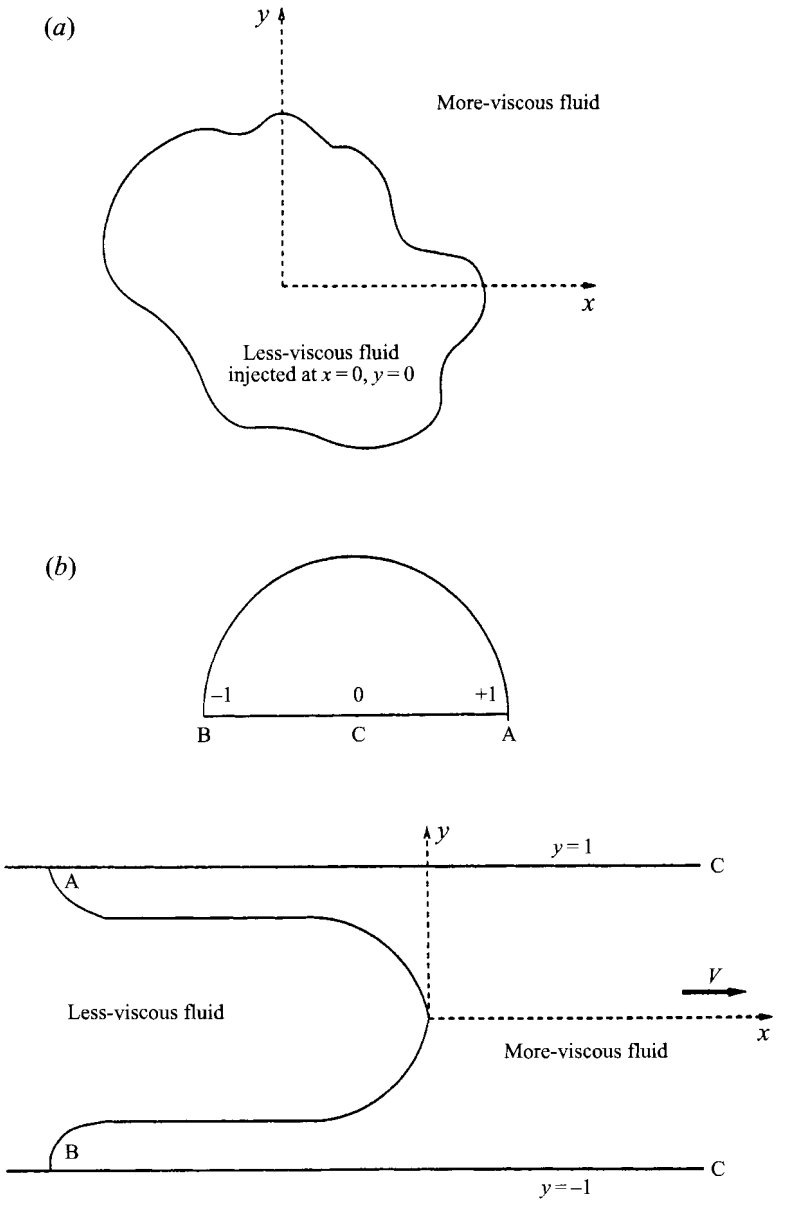

FIGURE 1. (*a*) Hele-Shaw flow in the radial geometry. (*b*) Flow in the channel geometry. The unit semicircle in the ζ-plane is mapped onto the viscous fluid region of the channel, with the circular arc being mapped to the interface. The points A, B, and C in the ζ-plane are mapped to the corresponding points in the channel.

the channel walls. The functional form of the conformal map is given by

$$z(\zeta, t) = -\frac{2}{\pi} \ln \zeta + \mathrm{i} + f(\zeta, t) \tag{4}$$

where we set the channel half-width $w = 1$; this is equivalent to non-dimensionalizing lengths by w. The requirement that z maps the diameter of the semicircle to the channel walls implies that $\mathrm{Im}\ f = 0$ on the diameter. We assume that the shape of

the extended finger obtained by reflection about each of the two sidewalls is smooth, entailing that f is analytic and $z_\zeta \neq 0$ in an open set containing the unit semicircle. The Schwartz reflection principle then implies that f is analytic and $z_\zeta \neq 0$ for $|\zeta| \leqslant 1$.

In either of these geometries, the fluid velocity $\boldsymbol{u}$, averaged across the plate gap, satisfies Darcy's law

$$\boldsymbol{u} = -\frac{b^2}{12\mu}\nabla p$$

where μ is the viscosity, b is the plate gap, and p is the pressure (here considered as a function of x and y). Thus $(-b^2/12\mu)p$ provides a velocity potential ϕ. Incompressibility implies the existence of a stream function ψ. We can therefore introduce a complex potential $W(z,t) = \phi + \mathrm{i}\psi$ which is an analytic function of z in the fluid region. Considered as a function of ζ, this potential is decomposed as

$$W(\zeta,t) = \frac{-Q}{2\pi}\ln\zeta + \mathrm{i} + \omega(\zeta,t) \tag{5}$$

where ω is assumed to be analytic in $|\zeta| \leqslant 1$. In the channel geometry, $Q = 4$ in order that the fluid velocity V far ahead of the finger equals unity. This is equivalent to normalizing fluid velocities by V. For the radial geometry, Q is the injection rate of air and will be taken as 2π. Furthermore, in (3) we choose $a(0) = 1$. Together with the value of Q, this makes our variables effectively dimensionless.

The interface conditions determine the evolution of the map $z(\zeta,t)$. The kinematic condition states that the motion of the interface in the normal direction is the same as the normal component of fluid velocity. For both the radial and channel geometries, this translates into

$$\mathrm{Re}\left\{\frac{z_t}{\zeta z_\zeta} - \frac{\zeta W_\zeta}{|z_\zeta|^2}\right\} = 0 \tag{6}$$

on $|\zeta| = 1$. The dynamic boundary condition (McLean & Saffman 1981) asserts that the pressure difference between the two sides of the interface is balanced by the product of surface tension and curvature. In either geometry, this statement corresponds to the condition

$$\mathrm{Re}\ \omega = \frac{-B}{|z_\zeta|}\mathrm{Re}\left[1 + \zeta\frac{z_{\zeta\zeta}}{z_\zeta}\right] \tag{7}$$

on $|\zeta| = 1$. Here B is a dimensionless surface tension parameter given by $B = b^2T/(12\mu Vw^2)$ in the channel geometry and $B = 2\pi b^2T/(12\mu Qa(0))$ in the radial geometry, where T is the surface tension.†

We note in passing that the boundary conditions (6) and (7) are simplified limits of much more complicated boundary conditions (Park & Homsy 1985; Reinelt 1987*a*) that account for the three-dimensional effects of a thin film left on the cell plates by the advancing interface. Studies of the more realistic boundary conditions in steady (Reinelt 1987*b*; Sarkar & Jasnow 1987; Schwartz & Degregoria 1987; Tanveer 1990) and time dependent (Tanveer 1995) flow show that, in many cases, the thin-film effects do not alter the qualitative features of the dynamics.

Equations (6) and (7) can be reformulated into a more convenient form for the purpose of numerical calculations. If we define $Z(v,t) = z(\mathrm{e}^{\mathrm{i}v},t)$, then it is easy to see using using well-known relations between the real and imaginary parts of an analytic

† Tanveer (1993) uses $B = b^2T/(3\mu Qa(0))$ and $Q = 4$ for the radial geometry.

function on the unit disk that (6) and (7) are equivalent to

$$Z_t = (H + \mathrm{i}Y)Z_v \tag{8}$$

where

$$\left.\begin{aligned} Y(v,t) &= \frac{Q}{2\pi|Z_v|^2}\left[1 - \frac{2\pi}{Q}\operatorname{Im}\omega_v\right], \\ H(v,t) &= \frac{1}{2\pi}\,PV\int_0^{2\pi} \mathrm{d}v'\,\cot\tfrac{1}{2}(v'-v)\,Y(v',t), \\ \operatorname{Im}\omega_v(v,t) &= \frac{B}{2\pi}\,PV\int_0^{2\pi} \mathrm{d}v'\,\cot\tfrac{1}{2}(v'-v)\,\frac{\partial}{\partial v'}\left[\frac{1}{|Z_v(v',t)|}\operatorname{Im}\frac{Z_{vv}(v',t)}{Z_v(v',t)}\right]. \end{aligned}\right\} \tag{9}$$

Note that H and $\operatorname{Im}\omega_v$ are just the (periodic) Hilbert transform of Y and of the derivative of the curvature, respectively; PV denotes principal value integral.

As explained in §1, to carry out the asymptotic calculations it is necessary to analytically continue the equations of motion to $|\zeta| > 1$. As a first step, we obtain the continuation of equations (6) and (7) into the domain $|\zeta| < 1$. This is done by employing the Poisson integral formula. In particular we use a variant of the standard formula which gives the value of an analytic function in the domain $|\zeta| < 1$ in terms of its real part evaluated on the unit circle. Using (6), this formula can be applied to the function $z_t/(\zeta z_\zeta)$ to yield (with appropriate choice of imaginary constant)

$$\frac{z_t}{\zeta z_\zeta} = I(\zeta,t) \tag{10}$$

for $|\zeta| < 1$, where

$$I(\zeta,t) = \frac{1}{4\pi\mathrm{i}}\oint_{|\zeta'|=1}\frac{\mathrm{d}\zeta'}{\zeta'}\frac{\zeta+\zeta'}{\zeta'-\zeta}\frac{1}{z_\zeta(\zeta',t)\tilde{z}_\zeta(1/\zeta',t)}\left[\zeta' W_\zeta(\zeta',t) + \frac{\tilde{W}_\zeta(1/\zeta',t)}{\zeta'}\right]. \tag{11}$$

Here the tilde is defined such that on $|\zeta| = 1$, $\tilde{F}(\zeta) = \overline{F(\bar{\zeta})}$, where F is a function analytic in a neighbourhood of the unit circle, and the overbar denotes complex conjugate. Thus, $\tilde{F}(1/\zeta)$ is the analytic extension of $\overline{F(\zeta)}$ off $|\zeta| = 1$. Note that if F is real on the real ζ-axis in the interval $(-1,1)$, then $\tilde{F} = F$. This is the case for the function z_ζ in the channel geometry, as well as for the symmetric radial solutions considered in this paper. Poisson's integral formula can be similarly applied to ω using (7), with the result that for $|\zeta| < 1$

$$\omega = -B\,J(\zeta,t), \tag{12}$$

where

$$\begin{aligned} J(\zeta,t) = \frac{1}{2\pi\mathrm{i}}\int_{|\zeta'|=1}&\frac{\mathrm{d}\zeta'}{\zeta'}\frac{\zeta+\zeta'}{\zeta'-\zeta}\frac{1}{z_\zeta^{1/2}(\zeta',t)\tilde{z}_\zeta^{1/2}(1/\zeta',t)} \\ &\times\left[1 + \frac{\zeta'}{2}\frac{z_{\zeta\zeta}(\zeta',t)}{z_\zeta(\zeta',t)} + \frac{1}{2\zeta'}\frac{\tilde{z}_{\zeta\zeta}(1/\zeta',t)}{\tilde{z}_\zeta(1/\zeta',t)}\right]. \end{aligned} \tag{13}$$

The choice of branch for the 1/2 power terms appearing in (13) should be consistent with the equality $|z_\zeta| = z_\zeta^{1/2}\,\tilde{z}_\zeta^{1/2}(1/\zeta)$ on $\zeta = \mathrm{e}^{\mathrm{i}v}$.

Equations (10)–(13) can now be analytically continued into the domain $|\zeta| > 1$ by deforming the contour in the ζ'-plane in the usual way, producing an additional term from the residue of the pole at ζ. (Note that analytic continuation to $|\zeta| = 1$

provides an alternative way to get (8), (9)). This leads to the following nonlinear integro-differential equation for z in the domain $|\zeta| > 1$:

$$z_t = q_1 z_\zeta + q_2 + B(2q_7(z_\zeta)_{\zeta\zeta}^{-1/2} + r), \tag{14}$$

where

$$q_1 = \zeta I(\zeta, t), \quad q_2 = \frac{-Q}{\pi} \frac{\zeta}{\tilde{z}_\zeta(1/\zeta, t)}, \quad q_7 = \frac{\zeta^3}{\tilde{z}_\zeta^{3/2}(1/\zeta, t)}, \tag{15}$$

and

$$r = q_3 + \frac{q_4}{z_\zeta^{1/2}(\zeta, t)} + \frac{q_5 z_{\zeta\zeta}(\zeta, t)}{z_\zeta^{3/2}(\zeta, t)}. \tag{16}$$

The precise form of q_3–q_5 is not crucial here; expressions for these terms are given on p. 166 of Tanveer (1993). The non-consecutive numbering of the q_i terms in (14) is used to conform to the notation used there.

In (14) we have singled out the surface tension term $Bq_7(z_\zeta)_{\zeta\zeta}^{-1/2}$, since this will be the most singular component of the equation for z in the neighbourhood of a zero of $z_\zeta(\zeta, 0)$. The function r contains surface tension terms which are less singular in this neighbourhood. We note for future reference that functions such as $I(\zeta, t), J(\zeta, t), \tilde{z}_\zeta(1/\zeta, t)$ and $\tilde{W}_\zeta(1/\zeta, t)$ are analytic in $|\zeta| > 1$. Since the functions $q_1(\zeta, t)$–$q_7(\zeta, t)$ depend only on these terms and their derivatives, they too are analytic in the region $|\zeta| > 1$ (except possibly at infinity).

Despite its complicated appearance, equation (14) is preferable for asymptotic studies of the effects of small surface tension. The reason is that the leading-order equation $z_t = q_1 z_\zeta + q_2$ is well-posed in $|\zeta| > 1$. (Tanveer 1993 provides analytical evidence for the well-posedness of this equation, whereas computational evidence is presented in Baker *et al.* 1995.) In contrast, the leading-order equation of the problem formulated in $|\zeta| \leqslant 1$ is ill-posed (Howison 1986*b*; Tanveer 1993).

2.1. *Outer perturbation expansion in powers of B*

The well-posedness of the zero-surface-tension problem in the extended domain $|\zeta| > 1$ allows the small-surface-tension problem $0 < B \ll 1$ to be studied perturbatively. This study has been initiated by Tanveer (1993), who examined the behaviour of the terms in an asymptotic expansion for z of the form (1) with initial data

$$z(\zeta, 0) = z_0(\zeta, 0). \tag{17}$$

Since the results are relevant in the present study, we summarize them here.

Upon substituting the expansion (1) into the evolution equation (14), it is seen that z_0 is simply the zero-surface-tension solution, while the equations for $z_1, z_2, \ldots$ contain singular forcing terms at points where $z_{0\zeta}$ is either singular or zero. The expansion (1) can break down at these points; in particular, this occurs near zeros and pole singularities in $z_{0\zeta}$ (these kinds of singularities are present in the initial data considered in §3). Formal asymptotic analysis suggests that the presence of surface tension modifies the singularity structure in inner regions near such points. However, in the case of pole singularities the modifications are restricted to a small ($O(B^{2/3})$) neighbourhood of the zero-surface-tension singularity, so that, in an outer asymptotic sense, the zero-surface-tension behavior is still relevant, i.e. $z_\zeta \sim A(t)/(\zeta - \zeta_s)$ for $B^{2/3} \ll |\zeta - \zeta_s| \ll 1$. Since it is known that pole singularities do not impinge on the unit circle in finite time when $B = 0$ (see Howison 1991), the modifications due to

small surface tension will not be felt by the physical interface in $O(1)$ times. Similar statements can be made about initial singularities of the form (2) with $\beta > 1/2$.

The situation is markedly different for initial zeros in z_ζ. Consider a simple zero in $z_\zeta(\zeta, 0)$ of the form

$$z_\zeta(\zeta, 0) \sim D(0)(\zeta - \zeta_0(0)) \tag{18}$$

with $|\zeta_0(0)| > 1$. For early enough times, the first-order term z_1 in a neighbourhood of $\zeta_0(t)$ takes the form

$$z_1 \sim A_0(t)(\zeta - \zeta_0(t))^{-3/2} + A_1(t)(\zeta - \zeta_d(t))^{-3/2} \tag{19}$$

with $A_0(0) + A_1(0) = 0$. In (19), $\zeta_d(t)$ satisfies

$$\dot{\zeta}_d(t) = -q_{1_0}(\zeta_d(t), t); \quad \zeta_d(0) = \zeta_0(0) \tag{20}$$

where a subscript 0 on any q_i denotes its evaluation using the corresponding $B = 0$ solution. The first term on the right-hand side of (19) balances the most singular forcing term $2\, q_{7_0}(z_{0\zeta})_{\zeta\zeta}^{-1/2}$ in the equation for z_1, and the second term is a solution of the homogeneous equation for z_1 and is required to satisfy the initial condition (17).

The singularity $\zeta_d(t)$ is termed a daughter singularity, even though it is not an actual singularity of z but rather of z^1, z^2, etc. The inner asymptotic analysis of Tanveer (1993) (summarized and extended in §4) suggests that, under some assumptions, a localized inner structure consisting of a cluster of $-4/3$ singularities resides in a neighborhood of each of $\zeta_d(t)$ and $\zeta_0(t)$. (Evidence presented later in this paper suggests that, at the time when $|\zeta_d| - 1 = O(B^{1/3})$, the cluster about $\zeta_d(t)$ begins to disperse.) The important feature here is that the motion of $\zeta_d(t)$, as specified by (20), is different from the motion of $\zeta_0(t)$, which is easily seen to be given by

$$\dot{\zeta}_0 = -q_1(\zeta_0(t), t) - q_{2\zeta}(\zeta_0(t), t)\left[z_{\zeta\zeta}(\zeta_0(t), t)\right]^{-1}. \tag{21}$$

This raises the possibility that z_ζ can differ significantly from $z_{0\zeta}$ as $B \longrightarrow 0$, even at points where $z_{0\zeta}$ is neither singular nor zero. In the following sections we examine this possibility in detail, through a comparison of asymptotic results and numerical computations.

3. Initial conditions and exact solutions for $B = 0$

We shall consider the effect of small non-zero B on a class of exact zero-surface-tension solutions for which z_ζ has a simple distribution of zeros and/or poles. The existence of exact solutions for $B = 0$ enables us to easily compare the zero- and non-zero-surface tension evolutions in numerical simulations and to check the asymptotically predicted scalings. Although the asymptotic analysis of Tanveer (1993) is quite general and can be applied to initial conditions for which there are no known exact $B = 0$ solutions (such as data $z_\zeta(\zeta, 0)$ with branch point singularities of the form (2)) it is clearly preferable to use data for which exact solutions already exist. We have found that many of the salient singular perturbation effects of surface tension appear even for this restricted class of initial data.

For the radial geometry, we consider initial data corresponding to the following exact $B = 0$ solution (Shraiman & Bensimon 1985):

$$z(\zeta, t) = \frac{A(t)}{\zeta}\left[1 + \frac{\zeta^3}{2\,\zeta_0^3(t)}\right] \tag{22}$$

$\xi_0(0)$	t_d	t_c
1.2	0.0463	0.3302
1.6	0.4455	3.709
2.0	1.101	15.50
2.4	1.949	47.28
2.8	2.970	119.97

TABLE 1. Comparison of the times t_d and t_c at which $\xi_d(t)$ and $\xi_0(t)$, respectively, reach the unit disk. The times are obtained by integrating (20) using the three-zero solution (22); we set $A(0) = 1$ and consider various values of $\xi_0(0)$.

where

$$A(t) = A(0)\zeta_0^3(0)\left[1 - \left(1 - \frac{2}{\zeta_0^6(0)} + \frac{1}{\zeta_0^{12}(0)} - \frac{4t}{\zeta_0^6(0)A^2(0)}\right)^{1/2}\right]^{1/2} \tag{23}$$

and

$$\zeta_0(t) = \zeta_0(0)\frac{A^{1/3}(0)}{A^{1/3}(t)}. \tag{24}$$

Here $A(0)$ and $\zeta_0(0)$ are real numbers satisfying $A(0) > 0$ and $|\zeta_0(0)| > 1$. This solution has three-fold symmetry and has three zeros of z_ζ outside the unit circle at positions where $\zeta^3 = \zeta_0^3(0)$. Exact solutions also exist for generalizations of (22) to n-fold symmetry. From the expression (22), it is easily seen that the initial zeros of z_ζ preserve their form but move to new locations given by $\zeta = \zeta_0(t)$, $\zeta_0(t)e^{2\pi i/3}$, and $\zeta_0(t)e^{4\pi i/3}$. Since $\zeta_0(t)$ monotonically approaches 1, the zeros move toward the unit disk. They impinge upon $|\zeta| = 1$ at a time $t = t_c$, where

$$t_c = \left[\frac{A(0)(\zeta_0^6(0) - 1)}{2\zeta_0^3(0)}\right]^2. \tag{25}$$

When the zeros reach the unit disk, the solution becomes singular and the interface develops cusps at three symmetric points. The equations and solution fail to make sense for $t > t_c$. For future reference, we note that expressions for q_{1_0}, q_{2_0}, and q_{7_0} are easily obtained by inserting the $B = 0$ solution (22) into (15); this gives

$$q_{1_0} = \frac{\zeta\zeta_0^6(1 + \zeta_0^3\zeta^3)}{A^2(\zeta_0^6 - 1)(\zeta^3\zeta_0^3 - 1)}, \quad q_{2_0} = \frac{2\zeta^2\zeta_0^3}{A(\zeta^3\zeta_0^3 - 1)}, \quad q_{7_0} = \frac{e^{i3\pi/2}\zeta_0^{9/2}\zeta^{9/2}}{A^{3/2}(\zeta^3\zeta_0^3 - 1)^{3/2}} \tag{26}$$

where we recall that the additional subscript 0 on q_1, q_2 and q_7 refers to the evaluation of these functions with $z = z_0$ and $\omega = 0$.

For non-zero B, the surface tension term in (7) becomes large when the interface nears cusp formation. Indeed, $B > 0$ calculations by Dai, Kadanoff & Zhou (1991) (using initial data corresponding to (22), with zeros close to the unit disk) show that the cusp is replaced by a small bulb of air protruding into the fluid, although in their calculations B is not small enough for the asymptotic theory to hold. As $B \to 0$, it might be surmised that capillary effects are not an important factor in the evolution until just before a cusp forms in the corresponding zero-surface-tension solution, z_0. However, the analysis of §2.1 suggests otherwise. Daughter singularities to the outer perturbation expansion are created at the positions of the initial zeros. These subsequently move towards the physical domain at a rate given to the leading order

by (20), with q_{1_0} given in (26). One can obtain a value for the theoretical daughter singularity impact time t_d by numerically integrating (20) up to the time at which $\zeta_d(t) = 1$. We have performed this integration for various $\zeta_0(0)$ (table 1) and find that $\zeta_d(t)$ reaches the unit disk much sooner than $\zeta_0(t)$. Thus, the daughter singularity clusters can have a significant effect on the interfacial evolution well before a zero of $z_{0\zeta}$ comes close to the unit disk, i.e. before the curvature in the zero-surface-tension solution is large. The detailed numerical computations given in §5 support the essential conclusions from asymptotics concerning the impact of daughter singularities and show the actual physical consequences of this impact.

For the channel geometry, we consider initial data corresponding to a family of exact $B = 0$ solutions (Saffman 1959) which is written in our formulation as

$$z(\zeta, t) = \mathrm{i} + d(t) - \frac{2}{\pi} \ln \zeta + \frac{2}{\pi}(1-\lambda) \ln \left(1 - \frac{\zeta^2}{\zeta_s^2(t)}\right) \tag{27}$$

where $1 < \zeta_s(0) < \infty$ and λ is a constant satisfying $0 < \lambda < 1$. The functions $\zeta_s(t)$ and $d(t)$ are determined by

$$\left.\begin{aligned} \lambda d - \frac{2}{\pi}(1-\lambda) \ln \zeta_s &= t + K_0, \\ d + \frac{2}{\pi} \ln \zeta_s + \frac{2}{\pi}(1-\lambda) \ln \left(1 - \frac{1}{\zeta_s^4}\right) &= K_1, \end{aligned}\right\} \tag{28}$$

where the constants K_0 and K_1 depend on the values of $\zeta_s(0)$ and $d(0)$. This solution corresponds to a single finger of air which is symmetric about the centreline of the channel, and which propagates into the liquid. Simple pole singularities in z_ζ are located at $\pm\zeta_s$; these produce the protrusions of liquid into air which define the sides of the finger. As $t \to \infty$, it is easily seen that $\zeta_s \to 1^+$ and $d(t) \sim t/\lambda$ and in this limit, one obtains a steady finger solution (Zhuravlev 1956; Saffman & Taylor 1958) of relative width λ, with tip speed

$$\frac{\mathrm{d}z}{\mathrm{d}t}(\zeta = \mathrm{e}^{\mathrm{i}\pi/2}) = \frac{1}{\lambda}. \tag{29}$$

When $0 < \lambda < 1/2$, a simple calculation based on (27) shows that the zeros of z_ζ are located on the imaginary axis at

$$\zeta_0 = \pm \mathrm{i}\zeta_s/(1-2\lambda)^{1/2}, \tag{30}$$

whereas for $1/2 < \lambda < 1$, they are located on the real axis at

$$\zeta_0 = \pm \zeta_s/(2\lambda - 1)^{1/2}, \tag{31}$$

further from $|\zeta| = 1$ than the singularities at $\pm\zeta_s$. The motion of the zeros, given by (30), (31), is always directed toward the unit circle $|\zeta| = 1$. However, unlike the examples in the circular geometry, as $t \to \infty$ the zeros settle down at positions a finite distance from $|\zeta| = 1$, i.e. $\zeta_0(t \to \infty) = \pm \mathrm{i}/(1-2\lambda)^{1/2}$ for $0 < \lambda < 1/2$, and $\zeta_0(t \to \infty) = \pm 1/(1-2\lambda)^{1/2}$ for $1/2 < \lambda < 1$. In fact, the asymptotic positions of the zeros can be thought of as parameterizing the asymptotic width of the finger, with $\lambda = 1/2$ when $\lim_{t\to\infty} \zeta_0(t) = \infty$.

For later use, we note that the insertion of the exact solution (27) into (15) gives

$$q_{1_0} = \frac{\pi\zeta\zeta_0^4\left[1 - 2\zeta_s^2\zeta_0^2 + \zeta_s^4 + \zeta^2(\zeta_0^2 + \zeta_s^4\zeta_0^2 - 2\zeta_s^2)\right]}{2\zeta_s^4(\zeta_0^4 - 1)(\zeta^2\zeta_0^2 - 1)}, \tag{32}$$

$$q_{2_0} = \frac{2(\zeta^2 - \zeta_s^{-2})}{(\zeta^2 - \zeta_0^{-2})}, \quad q_{7_0} = \frac{e^{i3\pi/2}\,\pi^{3/2}\,\zeta^{3/2}\,(\zeta_s^{-2} - \zeta^2)^{3/2}}{2^{3/2}(\zeta_0^{-2} - \zeta^2)^{3/2}}. \tag{33}$$

It is easy to deduce from (20) and (32) that there is a fundamental difference in the motion of $\zeta_d(t)$ between cases where $\lambda > 1/2$ and those where $\lambda < 1/2$. In the first case, the daughter singularities $\pm\zeta_d(t)$ are on the real ζ-axis, but are further away from $|\zeta| = 1$ than the poles located at $\pm\zeta_s(t)$. Since $\zeta_s(t)$ approaches but never reaches $|\zeta| = 1$ in finite time, the daughter singularities $\pm\zeta_d$ never reach $|\zeta| = 1$. In the second case, $\zeta_d(t)$ moves along the imaginary ζ-axis towards $\zeta = i$ and will reach this point at a finite time t_d. The precise value of t_d for given λ and $\zeta_s(0)$ can be easily computed by numerically integrating (20) up to the time at which $\zeta_d(t) = 1$.

The effect of small non-zero B on this class of exact solutions is expected to be particularly interesting since the limiting steady-state finger cannot have an arbitrary width λ. Instead, λ must satisfy the selection criteria $\lambda = \lambda_n(B)$ (Shraiman 1986; Combescot *et al.* 1986, 1987; Hong & Langer 1986; Tanveer 1987; Dorsey & Martin 1987), where $\lambda_n(B)$ is given to leading order by

$$\lambda_n(B) = \tfrac{1}{2}\left\{1 + \left(\tfrac{1}{8}\pi^2 C_n B\right)^{2/3}\right\}, \quad n = 0, 1, 2, \ldots. \tag{34}$$

The integer n parameterizes the family of solutions; the narrowest finger, which is the unique stable steady solution, corresponds to $n = 0$ and $C_0 = 1.47$ (Combescot *et al.* 1987; Dorsey & Martin 1987; Tanveer 1987). The steady finger shapes are given to leading order by (27) in the limit $t \to \infty$, when the above values of λ_n are substituted for the width λ.

An important issue in the dynamics is how the selected steady-state finger satisfying (34) is approached in time. More specifically, one would like to know how the transition time to the selected steady-state solution scales with B. In §5, we present evidence that this transition occurs in $O(1)$ time as $B \to 0$, as long as $\lambda < 1/2$. On the surface this may appear surprising, since the curvature in the $B = 0$ problem is not large and therefore the surface tension term, when evaluated on the interface, is small. However, the $O(1)$ transition time can be explained by considering the influence of the daughter singularity cluster as it approaches the physical domain in $O(1)$ time.

4. Inner equations

As was pointed out in §2.1, the perturbation expansion (1) is invalid near a zero ζ_0 of $z_{0\zeta}$ and near any daughter singularities. In the general initial value problem, Tanveer (1993) has derived and analysed nonlinear equations which are valid in an inner region about $\zeta_0(t)$, along with equations that are valid in an inner region about $\zeta_d(t)$ after it has separated from $\zeta_0(t)$. While the inner equations have not been explicitly solved, they provide us with important scaling information. In this section we summarize the analysis of Tanveer, and extend it to include late times when the daughter singularity effects are felt on the physical interface.

4.1. *Inner equations near a zero of* z_ζ

To obtain equations which are valid in the neighbourhood of a zero $\zeta_0(t)$, we introduce the inner variables

$$\left.\begin{aligned} \xi &= \frac{1}{k_1(t)}\frac{\zeta-\zeta_0(t)}{B^{2/7}}, \\ \tau &= B^{-2/7}\int_0^t \mathrm{d}t'\,\frac{k_1(t')q_{2_0\zeta}(\zeta_0(t'),t')}{k_2(t')}, \\ G(\xi,t) &= \frac{z-\int_0^t \mathrm{d}t' q_2(\zeta_0(t'),t')}{k_2(t)\,B^{4/7}}, \end{aligned}\right\} \tag{35}$$

where

$$k_1(t)=\frac{q_{7_0}^{2/7}(\zeta_0(t),t)}{q_{2_0\zeta}^{2/7}(\zeta_0(t),t)z_{0\zeta\zeta}^{1/7}(\zeta_0(t),t)}, \quad k_2(t)=\frac{q_{7_0}^{4/7}(\zeta_0(t),t)z_{0\zeta\zeta}^{5/7}(\zeta_0(t),t)}{q_{2_0\zeta}^{4/7}(\zeta_0(t),t)}.$$

These scalings produce a dominant balance between the first four terms of equation (14). The factors $k_1(t), k_2(t)$, $\int_0^t \mathrm{d}t'\ k_1(t')q_{2_0\zeta}(\zeta_0(t'),t')/k_2(t')$ and $\int_0^t \mathrm{d}t' q_2(\zeta_0(t'),t')$ are included in the scaling in order to obtain an equation for G which is devoid of coefficients that are functions of t. For the initial data of §3, it is easily verified from (26) and (33) that $\arg\tau = 0$ when t is real and positive.

To the leading order in B, equation (14) now reduces to

$$G_\tau = -G_\xi + \xi - 2\left[G_\xi^{-1/2}\right]_{\xi\xi}. \tag{36}$$

This equation is canonical, in the sense that it is valid near every initial zero for small times, provided the location of the initial zero is not too close to the unit circle. (More precisely, equation (36) is valid up to $t = O(B^{2/7})$, provided $|\zeta_0(0)| - 1 \gg B^{1/3}$.) The initial conditions imply that $G_\xi(\xi,0) = \xi$. In order for G_ξ to match with $z_{0\zeta}$ as $\zeta \to \zeta_0(t)$, it is necessary that $G_\xi(\xi,\tau) \sim \xi$ along sectors in the complex ξ-plane which are directed towards the physical domain.

Tanveer (1993) has analysed equation (36) with the given initial data and asymptotic boundary condition over several distinct ranges in τ and ξ. For each range, we summarize the important features.

(*i*) $\tau \ll 1$ (i.e. $t \ll B^{2/7}$): For this range of time, there is an asymptotic similarity solution to (36) which contains singularities of the form

$$G_\xi \sim A(\tau)[\xi - \xi_p(\tau)]^{-4/3}. \tag{37}$$

The location of a given singularity satisfies $\xi_p(\tau) = \tau - \eta_p\tau^{2/9}$, where η_p marks the position of the singularity in terms of the similarity variable $\eta = (\xi-\tau)/\tau^{2/9}$. Heuristic arguments suggest that there are infinitely many such singularities. Thus, a collection of $-4/3$ singularities in z_ζ is formed; initially, each of these coincides with $\zeta_0(0)$. However, the singularities move away from this point for $\tau > 0$.

(*ii*) $\tau = O(1)$ (i.e. $t = O(B^{2/7})$): When $\tau = O(1)$, the asymptotic ordering which leads to the similarity solution in stage (i) breaks down. To continue, it is necessary to solve (36) with the given initial condition and matching condition in the complex ξ-plane along time-dependent contours in ξ (required to make the problem well-posed). This appears to be an involved calculation, and is not attempted here.

(*iii*) $\tau \gg 1$ (i.e. $B^{2/7} \ll t \ll 1$), with $|\xi| \ll \tau$: The nature of the solution cannot be

determined with certainty in this range of time, since it depends on the solution at $\tau = O(1)$, which is unknown. One possibility is that, for $|\xi| \ll \tau$, the function $G_\xi(\xi, \tau)$ equilibriates to the steady-state solution of (36). This is plausible, since rewriting the outer perturbation expansion in the inner variables (for $1 \ll |\xi| \ll \tau$) causes the τ dependence to disappear at the same order as it does in the inner solution. However, this is not the case when $\xi - \tau = O(1)$, since there is a singularity of the outer perturbation expansion at $\xi = \tau$ corresponding to the daughter singularity at $\zeta = \zeta_d(t)$.

(*iv*) $\tau \gg 1$, with $\xi - \tau = O(1)$: When $\xi - \tau = O(1)$ there is an asymptotic similarity solution that again contains $-4/3$ singularities, i.e. $G_\xi \sim K(\tau)(\xi - \xi_q(\tau))^{-4/3}$ for $\tau \gg 1$ and for ξ sufficiently close to $\xi_q(\tau) = \mu_q \tau^{-1/6} + \tau$. Here μ_q is the location of a singularity in the similarity variable $\mu = (\xi - \tau)/\tau^{-1/6}$. In terms of ζ and z_ζ, we have

$$z_\zeta(\zeta, t) \sim \tilde{K}(t)(\zeta - \zeta_q(t))^{-4/3} \tag{38}$$

where

$$|\zeta_q(t) - \zeta_d(t)| = O(B^{1/3}) \tag{39}$$

and $\tilde{K}(t) = O(B^{4/9})$. Equation (39) follows from substituting of $\xi_0(\tau) = \mu_q \tau^{-1/6} + \tau$ into the first relation of (35) and using the fact that $\zeta_d = \zeta_0 + B^{2/7} k_1 \tau$. Assuming that the scalings in (38) and (39) hold even for $t = O(1)$, then the $-4/3$ singularities are clustered about a $B^{1/3}$-sized region around $\zeta_d(t)$, the daughter singularity in the outer perturbation expansion. This is important for our purposes, since the $B^{1/3}$ scale around a daughter singularity gives the size of inner region where $|z_\zeta - z_\zeta^0|$ is $O(1)$.

Unfortunately, we cannot verify whether the similarity solution in stage (iv) is the relevant solution without knowing stage (ii), i.e. the $\tau = O(1)$ solution. However, we do point out that the numerical calculations of §5 show behaviour that is not inconsistent with the scenarios given in stages 3 and 4.

For the channel initial condition corresponding to (27) with $\lambda < 1/2$, figure 2 illustrates the different stages in the evolution of the singularity clusters. Stages (i)–(iv) described above are shown schematically in part (*a*), which depicts the separation of the singularity cluster around $\zeta_d(t)$ from the inner region around $\zeta_0(t)$. Parts (*b*) and (*c*) of the figure are described below. We note that a similar diagram holds for $\lambda > 1/2$, except the entire process now occurs near zeros which lie on the real ζ-axis, rather than the imaginary ζ-line. For the radial initial condition corresponding to (22), each of the three initial zeros of z_ζ gives rise to an analogous process.

4.2. *Inner equations near a daughter singularity*

For $t = O(1)$, the daughter singularity $\zeta_d(t)$ is clearly at $O(1)$ distance from $\zeta_0(t)$ (figure 2*b*). Consequently, the zero-surface-tension solution $z_{0\zeta}(\zeta, t)$ is non-zero and regular near $\zeta_d(t)$. However, the outer asymptotic expansion breaks down at $\zeta_d(t)$. It is therefore useful to also consider inner equations valid in a neighbourhood of $\zeta_d(t)$. For this inner region, the appropriate choice of scaled variables is found to be $\tilde{\xi} = (\zeta - \zeta_d(t))/B^{1/3}$ and $Q(\tilde{\xi}, t) = (z_\zeta - z_{0\zeta}(\zeta_d(t), t))$; these scales are depicted in figure 2(*b*).† An inner equation for $Q(\tilde{\xi}, t)$ can then be obtained under the assumption that the distance of the daughter singularity $\zeta_d(t)$ from $|\zeta| = 1$ satisfies $|\zeta| - 1 \gg B^{1/3}$, so that it is consistent to approximate the global integral terms $q_1, q_2, \ldots$ etc. by $q_{1_0}, q_{2_0}, \ldots$.

† From (14), it might appear that the inner variables should be chosen as $\tilde{\xi} = (\zeta - \zeta_d(t))/B^{1/3}$ and $Q(\tilde{\xi}, t) = (z_\zeta - z_{0\zeta}(\zeta_d(t), t))/B^{1/6}$, where $Q(\tilde{\xi}, t)$ is required to match to the second term on the right-hand side of (19). However, for $\tau = O(1)$ this choice is inconsistent with the relations (38),(39) and with the numerics of §5, which show that $z_\zeta - z_{0\zeta}(\zeta_d(t), t)$ is $O(1)$ for ζ near ζ_d.

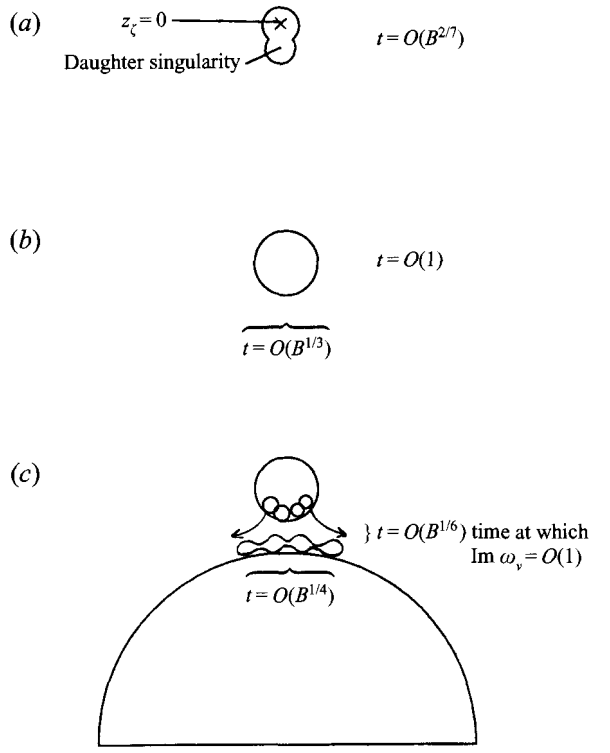

FIGURE 2. Diagram summarizing the relevant time and space scales in the evolution of a daughter singularity: (*a*) creation; (*b*) motion toward $|\zeta| = 1$; (*c*) 'impact' on $|\zeta| = 1$ (showing the break-up of the cluster into smaller subclusters). The half disk at the bottom of the figure represents the upper half of $|\zeta| = 1$.

The reader is referred to Tanveer (1993, equation (7.4)) for the specific form of this inner equation.

We now present new results which describe the stage where the distance of the 'outer' singularity satisfies $|\zeta_d(t)| - 1 \sim O(B^{1/3})$. At this time the edge of the daughter singularity cluster is in the proximity of the unit disk (this is the early portion in figure 2(*c*), where the singularity cluster is intact), and hence the leading-order inner equation for $Q(\tilde{\xi}, t)$ breaks down. We remark that this stage does not occur in $O(1)$ time for initial conditions where the daughter singularity motion is shielded by the motion of other singularities, as is the case for the channel initial condition corresponding to (27) with $\lambda > 1/2$.

When the daughter singularity is within $O(B^{1/3})$ of $|\zeta| = 1$, it is convenient to consider the spatial variable v defined by $\zeta = e^{iv}$. Introduce the scaled variables

$$\chi = \frac{v - v_d(t)}{B^{1/3}}, \quad T = \frac{t - t_d}{B^{1/3}}, \quad z_\zeta = R(\chi, T) \tag{40}$$

where $v_d(t) = \arg \zeta_d(t)$. In the specific problems we consider $v_d(t)$ is constant due to symmetry. The spatial scale is inherited from the previous stage of analysis, and reflects the notion that the $-4/3$ singularities are clustered about a $B^{1/3}$-sized region surrounding the daughter singularity. The $O(1)$ scale for z_ζ is selected by the requirement that it match to the zero-surface-tension solution as $\chi \to \pm\infty$. The time scale is then the only distinguished scale. We remark that these inner scales are

unaffected by the details of the hypotheses made in stages (iii) and (iv) of §4.1, as long as condition (39) holds.

In terms of the rescaled variables, the dynamic condition (7) becomes

$$\omega = B^{2/3}\,\Omega(\chi, T) \tag{41}$$

where

$$\Omega = -\frac{1}{|R|}\mathrm{Im}\left[\frac{R_\chi}{R}\right] - \mathrm{i}\mathscr{H}\left(\frac{1}{|R|}\mathrm{Im}\left[\frac{R_\chi}{R}\right]\right).$$

Here $\mathscr{H}$ is the Hilbert transform, defined as the principal value integral

$$\mathscr{H}(f) = \frac{1}{\pi}\,PV\int_{-\infty}^{\infty}\frac{f(y)}{x-y}\mathrm{d}y.$$

The kinematic equation (6) gives an evolution equation for R:

$$R_T = \left[\frac{\mathrm{i}(1 - B^{1/3}\mathrm{Im}\Omega_\chi)}{|R|^2} - \mathscr{H}\left(\frac{1}{|R|^2}\right) + B^{1/3}\mathscr{H}\left(\frac{\mathrm{Im}\Omega_\chi}{|R|^2}\right)\right]_\chi$$
$$+\mathrm{i}B^{1/3}\left[-\mathscr{H}\left(\frac{1}{|R|^2}\right) + \frac{\mathrm{i}}{|R|^2}\right]R + O(B^{2/3}) \tag{42}$$

where we have used the fact that $\mathrm{d}v_d/\mathrm{d}t = 0$, which holds for the symmetric initial value problems considered here.

To leading order, the evolution equation (42) becomes

$$R_T = \left[\frac{\mathrm{i}}{R^*} + \mathscr{H}\left(\frac{1}{|R|^2}\right)R\right]_\chi. \tag{43}$$

Interestingly enough, curvature terms do not appear at the leading-order, and equation (43) is therefore identical to the leading-order part of the zero-surface-tension equation ((8), with $B = 0$), once it is rewritten in terms of the rescaled variables. However, the solution to this inner equation differs from the zero-surface-tension solution $z_{0\zeta}$ by $O(1)$ because the inner region inherits the cluster of $-4/3$ singularities around $\zeta_d(t)$. The creation of singularities near an initial zero due to surface tension effects should now begin to be felt on the physical interface.

An equation analogous to (43) appears in the study of dendritic crystal growth. In that context, several relevant facts have been uncovered about the dynamics of singularities under (43) (Kunka, Foster & Tanveer 1996). In particular, for $T \gg 1$ it has been shown that singularities initially at $O(1)$ distance from the real χ-axis approach it like $c_1/T^{1/2}$, where c_1 is a constant, while the real-χ location of singularities goes asymptotically like $\pm c_2\ T^{1/2}$ for constant c_2. Thus, the daughter singularity cluster spreads out over the real χ-direction, but gets compressed in the Im χ direction (see figure 2*c*). For initial value problems such as the ones considered here, there is symmetry about Arg ζ = Arg ζ_d and so the line Re $\chi = 0$ acts as a separatrix: singularities to the left of this line will advect to the left, and vice versa. This behaviour has been demonstrated analytically for a cluster of pole singularities advecting toward a point of symmetry (Kunka *et al.* 1996). Using the method of Baker *et al.* (1995), similar behaviour has been numerically observed for branch point singularities.

Using this information, it is interesting to consider the deformation of the singularity cluster at the stage when the surface tension term becomes $O(1)$ in size. This deformation will later be quantified in the numerical calculations. From a rescaling of χ, it is clear that the surface tension term $B^{1/3}$ Im Ω_χ reaches $O(1)$ when the

singularities comprising the cluster are within $O(B^{1/6})$ of the real χ-axis. Since each singularity moves toward Im $\chi = 0$ like $c_1/T^{1/2}$, this distance is reached in a scaled time $T = O(B^{-1/3})$, which corresponds to an actual time $t - t_d = O(1)$. During this span the cluster disperses over a real-χ region of size $O(B^{-1/6})$, corresponding to a v interval of size $O(B^{1/6})$ (shown in the late stage in figure 2*c*). The numerical calculations of §5 suggest that, by this time, the singularity cluster has broken up into several subclusters.

At this point, the cluster of singularities within the original daughter singularity have dispersed enough so that the daughter singularity itself no longer exists in a well-defined form. Beyond this time, the analytical scaling results are not very revealing. They suggest that there are multiple subclusters with size scaling like $O(B^{1/2})$ in the v variable; each of these advects with $O(1)$ speed along the unit circle towards $\zeta = \pm 1$, which (in the case of Saffman finger initial data) corresponds to the tails of the finger. The $O(B^{1/2})$ size of the smallest expected length scale can also be obtained from a simple physical argument based on the linear dispersion relation of a near planar interface. After the singularity structures have moved towards the finger tails, the finger shape away from the tails evolves under (43) like a a zero-surface-tension solution, but one that is different from the zero-surface-tension solution we started with.

5. Numerical results

In this section we report the results of $B > 0$ numerical computations performed directly in the physical domain, using initial data corresponding to the exact $B = 0$ solutions described in §3. For each initial value problem, calculations are made for a sequence of decreasing B, and the results are compared with the known $B = 0$ solutions. The computations are used to reconcile the analytically predicted scalings, and to observe the physical consequences of daughter singularities as they approach the unit circle.

5.1. *Computations in the channel geometry*

For the $B = 0$ Saffman finger solution (27), the presence of pole singularities near the unit circle causes strong variation in the interfacial profile. Since the pole singularities are preserved in the outer asymptotic sense when $0 < B \ll 1$ and $t > 0$, simulations for non-zero B require a discretization that can properly resolve the indentations produced on the interface. We satisfy this requirement by employing a boundary integral method in which the interface is parameterized in terms of an equal-arclength variable α. More precisely, α has the property that if s measures arclength along the interface, then $s_\alpha(\alpha, t)$ is independent of α, and depends only on time. This kind of parameterization is attractive for a second reason: using it, Hou, Lowengrub & Shelley (1994) have been able to formulate a method that deals with the stiffness of the evolution equations in a particularly efficient manner. Their method relies on the use of the interface's tangent angle $\theta(\alpha, t)$ and its length $L(t)$, rather than its x and y positions, as the dynamical variables. For the channel geometry, $\theta(\alpha, t)$ is a periodic function of α since the effect of the sidewalls is equivalent to a periodic array of fingers. The equations of motion for θ and L are then reformulated, so that components of the high-order terms which are dominant at small scales are separated from the other terms, in such a way that they appear linearly (with constant coefficients). Then an implicit time integration method such as Crank–Nicholson, or a linear propagator method, can be applied in a straightforward manner. We use their algorithm in conjunction

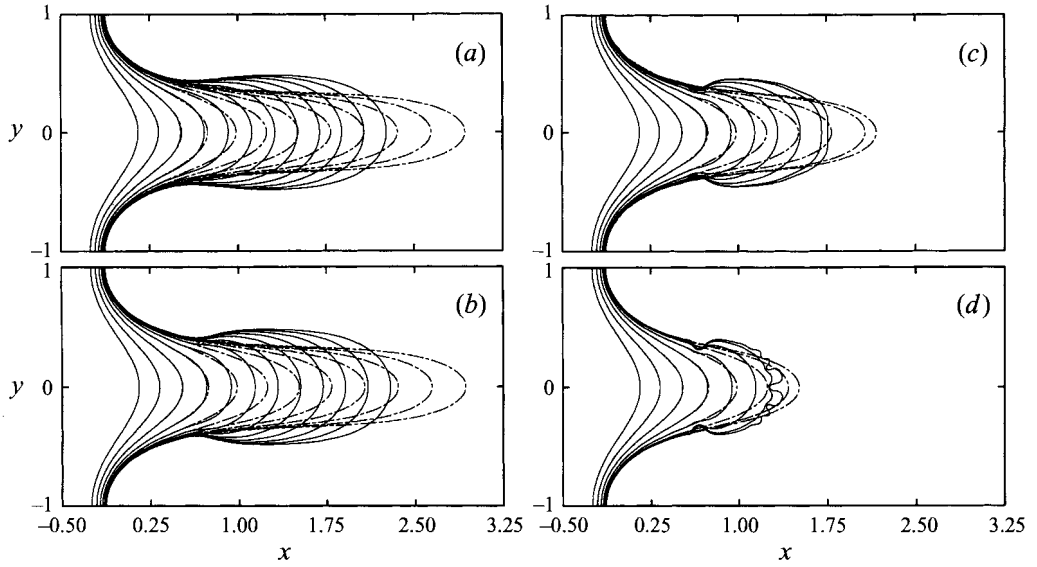

FIGURE 3. Evolution of a finger using an initial condition of the form (27) with $\lambda = 1/3$ and $\zeta_s(0) = 1.5$. The solid curves correspond to $\tilde{B}$ values (*a*) 0.01; (*b*) 0.0025; (*c*) 0.001; (*d*) 0.0005. The dashed profiles show the exact $B = 0$ solution. Here, the filter level is 10^{-13}. The time difference $\Delta\tilde{t}$ between profiles is 0.3, with the following exceptions: $\Delta\tilde{t} = 0.1$ for the last interval in (*c*), and $\Delta\tilde{t} = 0.2$ and 0.1 for the last two intervals in (*d*).

with a linear propagator method which is second order in time. Spatial discretizations are chosen to be spectrally accurate. We refer the reader to Hou *et al.* (1994) for a detailed description of the method.

For each calculation that we perform, a sufficient number of discretization points are used so that all Fourier modes of $\theta(\alpha, t)$ with amplitude exceeding round-off error are well resolved. For small values of surface tension, spectral filtering (Krasny 1986) is employed to prevent the spurious growth of short-wavelength modes generated by round-off error. As soon as the magnitude of the highest-wavenumber coefficient exceeds the filter level, the number of modes is doubled, with the additional modes given an initial amplitude of zero. The time step Δt is decreased until there are no detectable differences in the solution within plotting accuracy, nor any significant differences in other quantities of interest. In a typical run, we begin with 512 points and use a time step of $\Delta t = 0.0025\pi^{-1}$. The factor of π^{-1} is a consequence of a scale change that is required for the numerically computed values to conform to the non-dimensionalization used here for the channel geometry. For convenience, numerical values in this subsection will be specified in terms of the scaled variables

$$\tilde{t} = \pi t; \quad \tilde{B} = \pi^2 B.$$

Figure 3 shows the interfacial profiles produced by Saffman finger initial data of the form (27), with $\lambda = 1/3$, $\zeta_s(0) = 1.5$ and $d(0) = 0$. These particular values for λ and $\zeta_s(0)$ are merely chosen to be representative; other $0 < \lambda < 1/2$ and $1 < \zeta_s(0)$ lead to qualitatively similar results. Solutions are shown for a sequence of decreasing B, with the $B = 0$ exact solution plotted for comparison. The filter level is set to 10^{-13}. The theoretical daughter singularity impact time corresponding to these data, obtained by the procedure described in §3, is $\tilde{t}_d = 0.757$. In the calculation with the largest value of surface tension (figure 3*a*), the $B = 0$ and $B > 0$ solutions show good

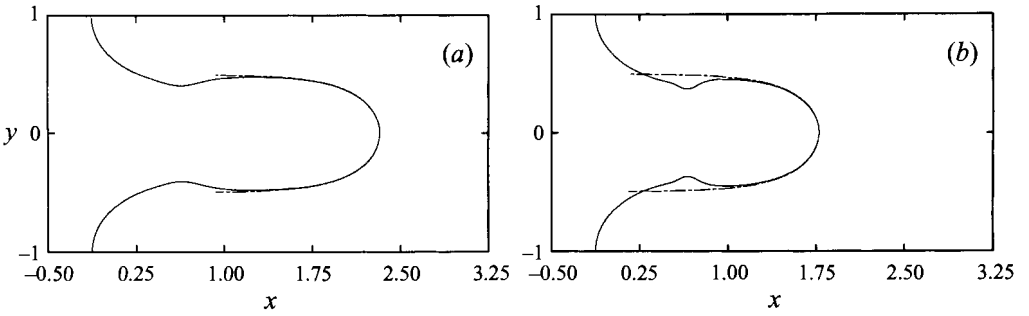

FIGURE 4. Comparison of the computed fingers (solid curves) for the initial condition of figure 3 with the corresponding steady state shape, given by (27),(34) in the limit $t \to \infty$. (*a*) $\tilde{B} = 0.0025$ solution, shown at time $\tilde{t} = 3.34$. The filter level for the calculation is 10^{-13}. (*b*) $\tilde{B} = 0.001$ solution, shown at time $\tilde{t} = 2.48$. Here the filter level is set to 10^{-25} (using 128-bit arithemetic) to avoid the branching at the fingertip which is evident in figure 3*c*.

agreement until approximately the fourth curve shown (corresponding to $\tilde{t} = 0.9$), after which the non-zero-surface-tension solution smoothly widens. Eventually, the solution approaches the selected steady finger shape (see figure 4), with a relative width λ_0 given by the formula (34). When B is reduced by a factor of 4 (figure 3*b*), similar behaviour is observed, with the exception that the widening process appears to occur somewhat more abruptly. This is most easily seen by comparing the sides of the fingers in figures 3*a* and 3*b*. As B is further reduced (figures 3*c* and 3*d*), this trend continues: the $B = 0$ and $B > 0$ solutions agree up until approximately the fourth curve ($\tilde{t} = 0.9$), after which the non-zero-surface-tension solution widens in an even more abrupt manner. Our objective is to accurately measure, in the limit $B \to 0$, the time at which the $B = 0$ and $B > 0$ solutions 'first' differ, as well as the time it takes for the $B > 0$ solution to widen into the selected steady shape.

Unfortunately, for the smaller values of B considered in figures 3(*c*) and 3(*d*), the solution develops branching at the tip of the finger before it can fully widen into the selected steady shape. It is easily seen that the branching is due to round-off-induced perturbations (i.e. noise) in the high-wavenumber modes, which quickly grow and appear as ripples in the solution. This is at once verified by redoing the computations in 128-bit arithmetic (e.g. double precision arithmetic on a Cray YMP), whereupon the onset of interfacial oscillations is delayed. The reason is that the use of a higher machine precision introduces the spurious perturbations at a lower amplitude, and reduces the noise-induced error. More generally, one can check for the presence of noise effects in a computed solution by redoing the computation with perturbed initial data of the form

$$z(e^{iv}, 0) = i\left(1 - \frac{2v}{\pi}\right) + \sum_{k=0}^{M}(\hat{z}_k(t) + \epsilon)e^{ikv} + \sum_{k=M+1}^{N} \hat{z}_k(t)e^{ikv} \tag{44}$$

where ϵ is slightly larger than the filter level. At times for which the two computations differ, perturbations at the size of machine round-off have grown enough to contaminate the results. An example of this procedure is given in figure 5, in which the $\tilde{B} = 10^{-3}$ computation of figure 3(*c*) is recomputed using perturbed initial data of the form (44), with $M = 27$ and $\epsilon = 1 \times 10^{-12}$. The two solutions agree well until the time $\tilde{t} = 2.1$, but soon after this the effects of the perturbations are evident. We

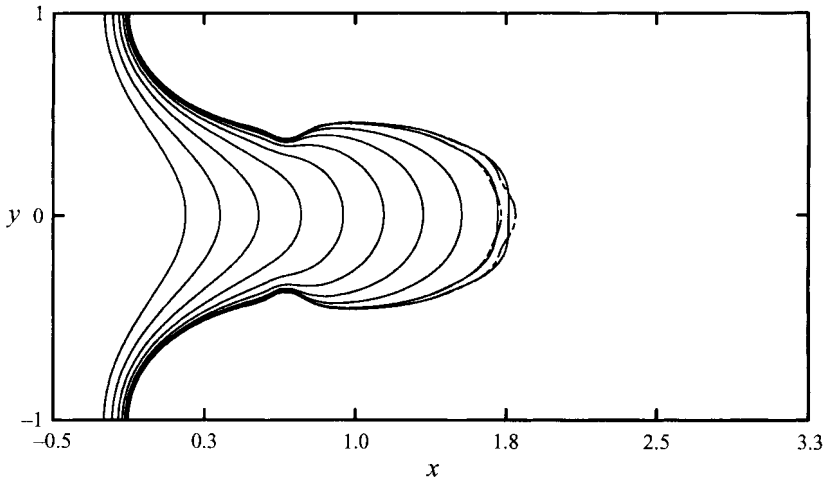

FIGURE 5. Comparison of the $\tilde{B} = 0.001$ computation in figure 3*c* (solid line) and a solution with perturbed data of the form (44) (dashed-line). We choose $\epsilon = 1 \times 10^{-12}$ and $M = 27$. The time difference $\Delta\tilde{t}$ between profiles is 0.3, except for the last two curves, where it is 0.1. Up to time $\tilde{t} = 2.1$, the two solutions plot on top of each other.

note that a similar procedure was used by Dai & Shelley (1994) in their examination of branching in the radial geometry.

The presence of such noise can adversely affect the desired comparison between asymptotics and numerics. We elaborate this point further. If terms like $a_n(t)\ln(1 - \zeta^2/\zeta_n^2(t))$ are added to (27) (corresponding to additional singularities), then for $|a_n(0)| \ll 1$ there will be no significant change in the initial interfacial shape. This amounts to adding noise to the data. However, this addition changes the initial condition in the complex plane and significantly affects the interface shape at later times, when $|\zeta_n(t)| \to 1$. To distinguish the dynamics that are inherent in the specified complex initial conditions from those due to noise, we use to the following procedure:

(*i*) Each computation is performed twice: once in 64-bit arithmetic with a filter level of 10^{-13}, and once in 128-bit arithmetic with a filter level of 10^{-25}. As long as these calculations agree to some prescribed tolerance, noise effects are negligible. Unless otherwise noted, all figures show results for the 10^{-25} filter level computations.

(*ii*) For values of B and times in which the above calculations differ, we perform a second 128-bit computation using perturbed data of the form (44). The perturbation size ϵ is chosen as 10–100 times the filter level, and M is set large enough to at least perturb all of the modes in the initial data which are above the filter level. As long as the two 128-bit calculations do not differ, they will be considered to be free of noise effects. In situations for which the two calculations differ measurably, error estimates will be included in relevant plots to give some indication of the possible influence of noise.

(*iii*) In many cases the 128-bit calculations were also repeated with a slightly higher filter level. This is somewhat analogous to reperforming the calculations with perturbed data. Again, as long as the calculations agree, noise effects are deemed absent.

We now discuss our measurement of the onset time for deviations between the $B = 0$ and $B > 0$ solutions. The strategy used is to compare the tip speed of the $B = 0$ solution to that for solutions with $B > 0$. This is done for a decreasing

sequence of B in the interval $[10^{-6}, 10^{-3}]$. The time at which the $B = 0$ and $B > 0$ quantities differ by a prescribed amount then provides a measure of the onset time for that particular value of B. Unfortunately, for $B < 1.0 \times 10^{-6}$, 128-bit arithmetic is not sufficient to prevent noise from contaminating the calculations before the desired onset time. Therefore, the results need to be extrapolated to $B \to 0$. The outcome of this extrapolation will be checked against the predicted daughter singularity impact time. We have found that tip speed provides an adequate measure of the onset time, since the daughter singularity in the upper half-plane moves along the imaginary axis and impinges upon the unit disk at $\zeta = \mathrm{i}$, which corresponds to the fingertip. In addition, it is easy to continuously monitor tip quantities during a calculation, whereas global comparisons of the zero- and non-zero-surface-tension solutions are difficult to obtain owing to the different parameterizations of these solutions. Although it is possible to convert from the equal-arclength parameterization to the conformal map parameterization at any given time in the evolution, this is difficult to do accurately for deformed interfaces such as those considered here. In any case, we have found the tip quantities to be sufficient for our present purposes.† Later, in the radial geometry, global comparisons between the $B = 0$ and $B > 0$ solutions will be obtained and used to corroborate many of the asymptotically predicted scalings.

An expression for the tip speed is obtained by evaluating equation (8) at $v = \pi/2$. Note that $H(\pi/2, t)$ is zero from symmetry. Consequently, the difference between the $B > 0$ and $B = 0$ tip speeds can be written as

$$Z_t(\pi/2, t) - Z_{0t}(\pi/2, t) = \frac{\mathrm{i}(\overline{Z}_v - \overline{Z}_{0v})}{\overline{Z}_v \overline{Z}_{0v}} + \frac{\mathrm{i}\,\mathrm{Im}\ \omega_v}{\overline{Z}_v}. \tag{45}$$

Define t_p to be the time required for the two tip speeds in (45) to differ by p in magnitude. According to asymptotic theory (specifically, see the discussion following equation (43)) the right-hand side of (45) should reach $O(1)$ in magnitude when the edge of the $O(B^{1/3})$- sized daughter singularity region reaches the unit disk, i.e. when $|\zeta_d(t)| - 1 = O(B^{1/3})$ (figure 2*c*). This implies that t_p will vary linearly with $B^{1/3}$ in the limit $B \to 0$, assuming that p is small enough so that only the leading edge of the daughter singularity cluster has reached the unit disk at the time t_p, i.e. the cluster has not yet begun to advect around $|\zeta| = 1$.

Figure 6 shows a plot of $\tilde{t}_p$ versus $B^{1/3}$, for $p = 0.0005$, 0.001, 0.002, 0.005, and 0.01. As expected, for each value of p that is sufficiently small, the marker points fall on a line which intersects the $B = 0$ axis near the daughter singularity impact time. Linear extrapolation of the four lower curves to $B = 0$ (using the two leftmost points on each curve) gives limiting onset times $\tilde{t}_p(B \to 0) = 0.762 \pm 0.005$, 0.785 ± 0.005, 0.776 ± 0.005 and 0.753 ± 0.01 for $p = 0.0005$, 0.001, 0.002, and 0.005, respectively. These values agree extremely well with the predicted daughter singularity impact time $\tilde{t}_d = 0.757$, shown as a half-cross in the figure. The error intervals in the onset times represent the estimated influence of noise. These are obtained by comparing values of $\tilde{t}_p$ for perturbed data of the form (44) (with ϵ set to 10^{-23}) to those for the unperturbed data. All other error intervals reported in this subsection are obtained similarly. For the range of B and p shown, the $\tilde{t}_p$ positions of the marker points change by less

† We have also numerically obtained the conformal map solution $z(v, t)$ using a method described in §5.2. In addition to providing a useful check on the present method, this solution can be used to obtain global comparisons between $z(v, t)$ and the zero-surface-tension solution $z_0(v, t)$, although for a narrow range of B. The results are completely consistent with those obtained using tip quantities.

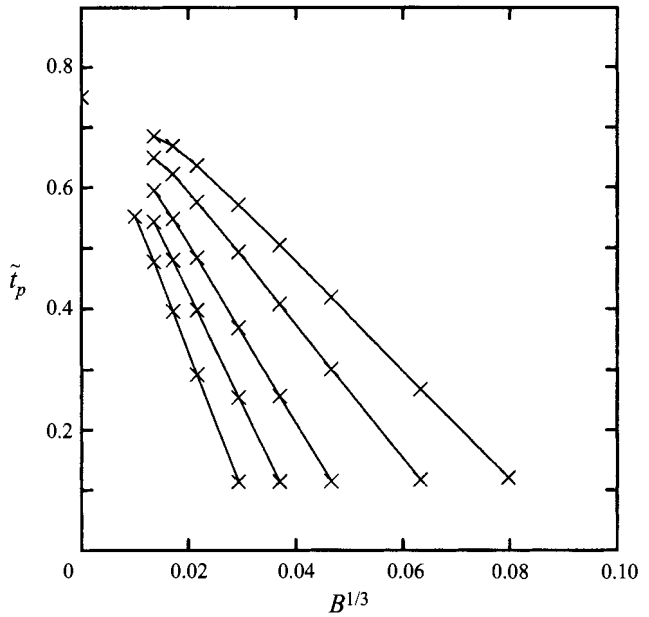

FIGURE 6. The time $\tilde{t}_p$ required for a deviation of size p between the $B > 0$ and $B = 0$ tip speeds, plotted versus $B^{1/3}$. We use the initial condition of figure 3. The filter level is 10^{-25}. From top to bottom, $p = 0.01$, 0.005, 0.002, 0.001, and 0.0005. The theoretical daughter singularity impact time is marked by a half-cross on the $B = 0$ axis. Linear extrapolation of the four lower curves to $B = 0$ (using the two leftmost points on each curve) leads to limiting values $\tilde{t}_p(B \to 0) = 0.762 \pm 0.005$, 0.785 ± 0.005, 0.776 ± 0.005 and 0.753 ± 0.01 for $p = 0.0005$, 0.001, 0.002, and 0.005, respectively. The error intervals gauge the variation in the positions of the $B = 0$ intercepts when perturbed data of the form (44) (with $\epsilon = 10^{-23}$) are used.

than 0.003 when the perturbed data are used. However, for a given p this variation increases quickly when B is decreased below the values shown in the figure.

Note that there is some flattening of the large-p curves for small values of B. Although part of this can be attributed to noise effects, the bulk of the flattening is likely due to the advection of the daughter singularity cluster about the unit disk. This can occur before $\tilde{t}_p$ is reached when p is sufficiently large and B is small enough. In this case, the p-sized deviation no longer occurs when the edge of the daughter singularity cluster reaches the unit disk, but rather occurs later, after the cluster has distorted. Thus, we do not expect a clear linear relationship between t_p and $B^{1/3}$ for larger values of p.

These details aside, it is clear from figure 6 that the curves corresponding to various values of p approach each other with decreasing B. Thus, the interval over which the zero- and non-zero-surface-tension solutions begin to veer away from each other becomes more localized in time as $B \to 0$. Furthermore, the location of this interval is consistent with the predicted daughter singularity impact time.

A more stringent check of the $B^{1/3}$ spatial scale for the daughter singularity cluster is obtained by considering a log-log plot of $\tilde{t}_d - \tilde{t}_p$ versus B, for various values of p. This is shown in figure 7. Only small values of p are considered, to guarantee that the daughter singularity is not significantly distorted due to advection around the unit disk at the time $\tilde{t}_p$. The curves in the figure indicate a linear relationship between $\tilde{t}_d - \tilde{t}_p$ and B^α, where α is determined by the slopes. The slope of each curve, computed using the two smallest-B points, is indicated in the figure. These values

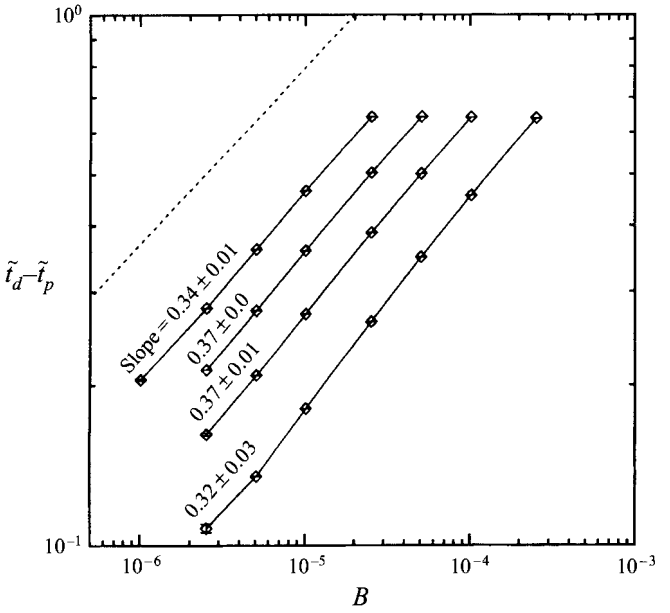

FIGURE 7. Log-log plot of $\tilde{t}_d - \tilde{t}_p$ versus B. The solid curves correspond to (top to bottom) $p = 0.0005$, 0.001, 0.002, and 0.005. The dashed line exhibits the theoretically predicted slope of 1/3. The error bars are obtained by comparing the results for perturbed initial data of the form (44) (with $\epsilon = 10^{-23}$) to those for unperturbed data. The slope of a line through the last two points on each curve is indicated in the figure, along with an error interval showing the variation in each slope when perturbed data are used.

compare well with the theoretically predicted slope of 1/3, which is exhibited by the dashed line in the figure. The small error bars on the left side of the figure show how the plotted values change when the perturbed data are used. The figure only includes those values of B for which this variation is not too large.

The tip speed is also useful for quantifying the time required for the finger to eventually fatten into its selected steady-state width $\lambda_0(B)$. In the time-dependent problem the width of the finger is not a uniquely defined quantity as it varies along the length of the channel. To get around this problem, we define the instantaneous 'width' of the finger to be the reciprocal of the tip speed, i.e.

$$A(t) = \left[\frac{\mathrm{d}z}{\mathrm{d}t}(\zeta = \mathrm{e}^{\mathrm{i}\pi/2}, t)\right]^{-1}. \tag{46}$$

This definition is motivated by the relation (29), from which it follows that $\lim_{t\to\infty} A(t) = \lambda_0$.

Figure 8 shows a plot of the instantaneous width $A(t)$ versus time, for a decreasing sequence of B. The $B = 0$ width is also plotted, and the daughter singularity impact time $\tilde{t}_d$ is indicated by a cross placed on this curve. The $\tilde{B} = 0.0001$ curve, marked E, is shown only up to time $\tilde{t} = 0.91$, since noise effects become prominent soon after that time. To the left of the figure it is seen that, as B is decreased, the non-zero-surface-tension width becomes increasingly more faithful to the zero-surface-tension width for times satisfying $t < t_d$. Shortly after the time t_d, the $B > 0$ curves suddenly veer in a direction corresponding to the fattening of the finger. The trend of the curves provides a graphic indication that the $B \to 0$ dynamics approaches the $B = 0$ dynamics when $t < t_d$, but drastically differs for $t > t_d$. At the far right of the plot,

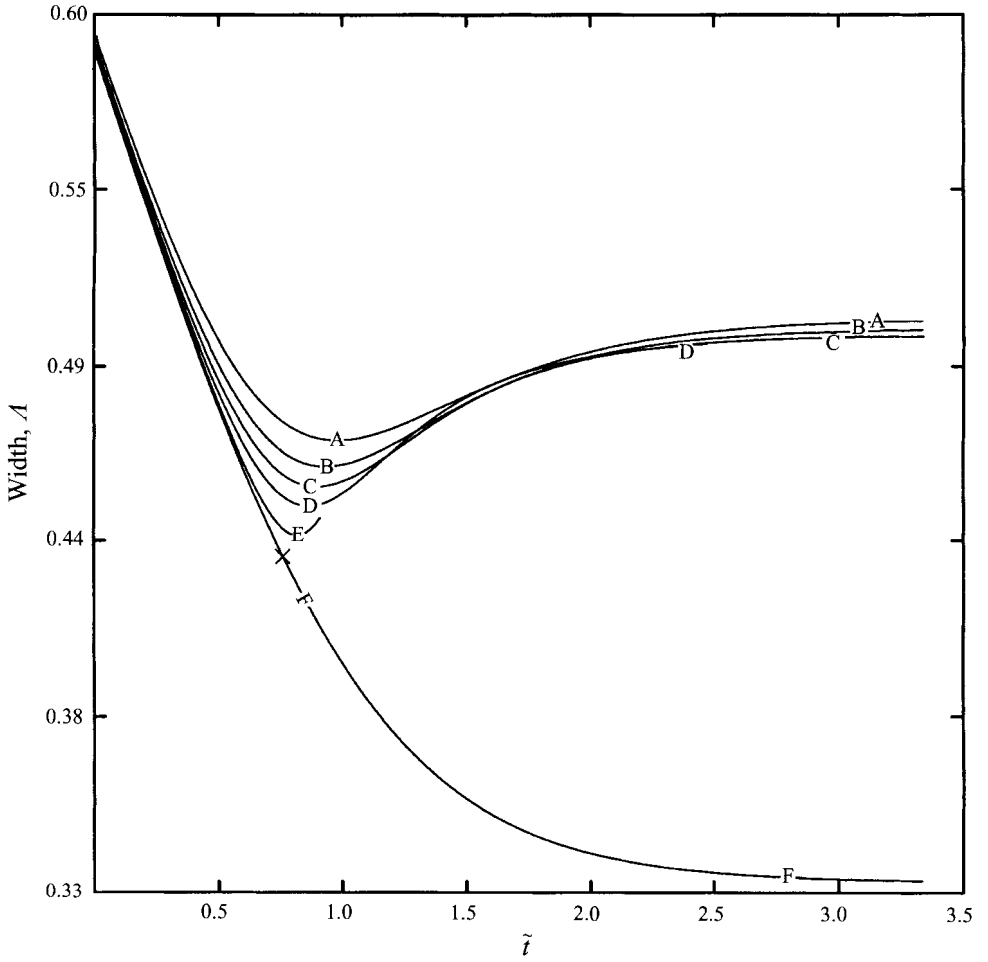

FIGURE 8. Plot of the width Λ versus $\tilde{t}$, for a decreasing sequence of B. The curves correspond to $\tilde{B}$ values 0.01 (curve A), 0.005 (B), 0.0025 (C), 0.001 (D), 0.0001 (E), and 0 (F). The theoretical daughter singularity impact time is indicated by the $\times$ placed on the $B = 0$ curve. Curve E is truncated before noise effects become prominent.

each curve approaches the steady-state width corresponding to the given value of B, i.e. $\Lambda(t) \to \lambda_0(B)$ where $\lambda_0(B)$ is given by (34). From the figure, it is apparent that once the curve starts to veer, the *rate* at which the instantaneous width approaches $\lambda_0(B)$ actually increases slightly as B is made smaller. This is most readily apparent during the time interval $0.8 < t < 1.5$.

The time required for the finger to widen can be further quantified by considering the ratio

$$\delta = \frac{\Lambda(t) - \lambda_0(B)}{\lambda_0(0) - \lambda_0(B)}, \tag{47}$$

where $\lambda_0(0) = 1/3$ is the steady-state width of the $B = 0$ solution. An example of the correspondence between this ratio and the actual degree to which the time-dependent and steady-state shapes match is provided by figure 4: the profile in figure 4*a* corresponds to $\delta = 1.1 \times 10^{-2}$, whereas that in figure 4*b* corresponds to $\delta = 1.7 \times 10^{-2}$. Now, consider the time t_w required for δ to reach the value w. In figure 9, we plot $\tilde{t}_w$ versus B for $w = 0.1, 0.05$ and 0.02. Since relatively long runs must be

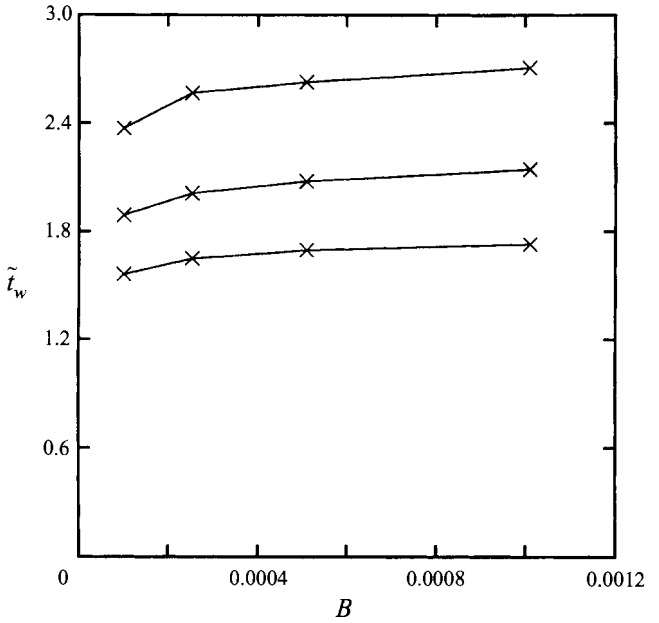

FIGURE 9. The time $\tilde{t}_w$ required for the relative difference δ between the steady and time-dependent widths to reach a value w, plotted versus B. The curves correspond to (top to bottom) $w = 0.02$, 0.05, and 0.1.

performed to obtain data for the plot, B cannot be taken too small, or noise effects will contaminate the results. Despite this, the range of B we do consider is sufficient to suggest that the time to widen decreases slightly as B is made smaller. Our data lead us to conclude that the daughter singularity produces the transition from an arbitrary thin-finger ($0 < \lambda < 1/2$) solution to one with a steady width determined by (34) in $O(1)$ time for $B \ll 1$.

Other values of $\lambda < 1/2$ lead to results that are qualitatively similar to those for $\lambda = 1/3$. In general, for data of the form (27) with fixed $\zeta_s(0)$, smaller values of λ produce daughter singularities that are initially closer to the unit disk and which have larger values of $|q_1(\zeta_d(t))|$. Thus, the effects of the daughter singularity (including the finger widening) occur sooner.

It is interesting to contrast the above results to those obtained for 'fat' finger initial data with $1/2 < \lambda < 1$. For λ in this range and $B = 0$, the zeros of z_ζ lie on the real line at positions given by (31). As discussed in §3, the daughter singularities in this case are prevented from reaching $|\zeta| = 1$ by the poles $\pm\zeta_s(t)$, which only approach ± 1 exponentially. Therefore, the $O(B^{1/3})$ inner neighbourhood around each daughter singularity will not affect the dynamics on $|\zeta| = 1$, at least until $t = O(-\ln B)$. Before this time, we expect the interface to be uninfluenced by the presence of the daughter singularities.

Computational evidence supporting this contention is difficult to obtain, since long-time computation requires us to suppress initial round-off errors below machine precision. However, for the period of time over which noise effects can be suppressed, numerical simulations give results that are consistent with this scenario. For example, figure 10 exhibits the results of a simulation with $\lambda = 2/3$ Saffman finger initial data, for $\zeta_s(0) = 1.5$ and $\tilde{B} = 0.0025$. The $B = 0$ and $B > 0$ solutions plot on top of each other until late stages of the evolution, when noise effects are felt. The difference in

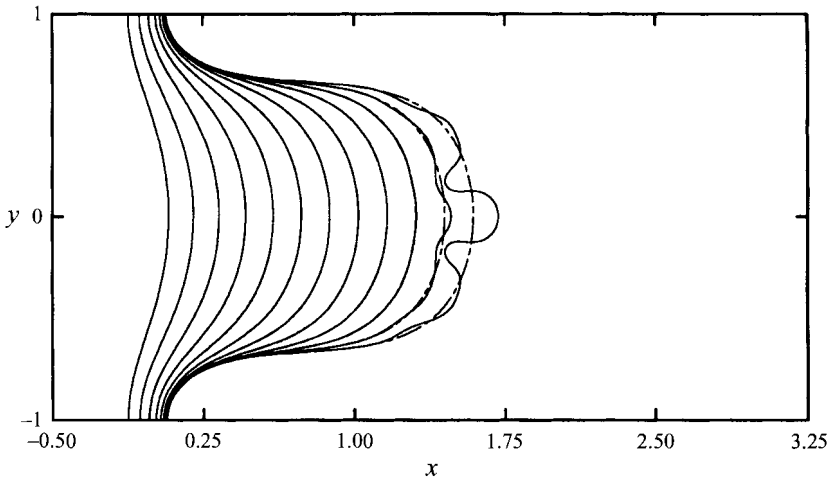

FIGURE 10. Evolution of a finger using initial data of the form (27) with $\lambda = 2/3$ and $\zeta_s(0) = 1.5$. The two sets of curves correspond to the $\tilde{B} = 0.0025$ computed solution (solid curves) and the $B = 0$ exact solution (dashed curves). Here, the filter level is 10^{-13}. The time difference $\Delta\tilde{t}$ between profiles is 0.3. The two solutions plot on top of each other until approximately $\tilde{t} = 2.7$, at which time noise effects cause branching in the computed solution.

tip curvature between the two solutions stays below 10^{-3} in magnitude for $\tilde{t} < 2.02$. It may at first appear that this result is inconsistent with the $B > 0$ steady-state theory. However, the steady-state selection result (34) shows that for small B, there exists a steady solution with width $\lambda_n(B)$ close to an arbitrary width $\lambda \in (1/2, 1)$, as long as n is sufficiently large. This steady state is linearly unstable to tip-splitting modes, although suppressing noise in the computation apparently prevents the instability from being activated. Thus, the finger of width $\lambda = 2/3$ can be achieved over a long period of time.

5.2. *Computations for the radial geometry*

We turn now to the radial geometry and consider initial data corresponding to (22), which contains three zeros of z_ζ in the region exterior to $|\zeta| = 1$. Long-time computations of the $B > 0$ evolution for these initial data, using the method of Hou *et al.* (1995), show that the $B = 0$ and $B > 0$ solutions differ significantly on the parts of the interface where the zero-surface-tension solution eventually forms a cusp (figure 11). Figure 11(*a*) compares the early stages of evolution between the exact $B = 0$ solution and the solution for $B = 0.00025$. The deviation between the two solutions is qualitatively similar in appearance to that for the channel geometry, and occurs before the curvature of the interface has become very large. The zero-surface-tension solution goes on to form cusps at locations corresponding to the vertices of the triangle. (For the initial data in figure 11 this occurs at time $t_c \approx 2.37$). In contrast, each cusp is replaced by a growing bulb of air in the $B = 0.00025$ solution. The bulbs are susceptible to noise-induced perturbations and eventually develop fingers and other branching structures, as seen in figure 11(*b*). As in the channel geometry, we perform a sequence of simulations for decreasing B to show that the onset of deviations between the $B = 0$ and $B > 0$ solutions is related to the impact of a daughter singularity cluster on the unit disk. We also use the computations to examine several of the predicted scalings given in §4.

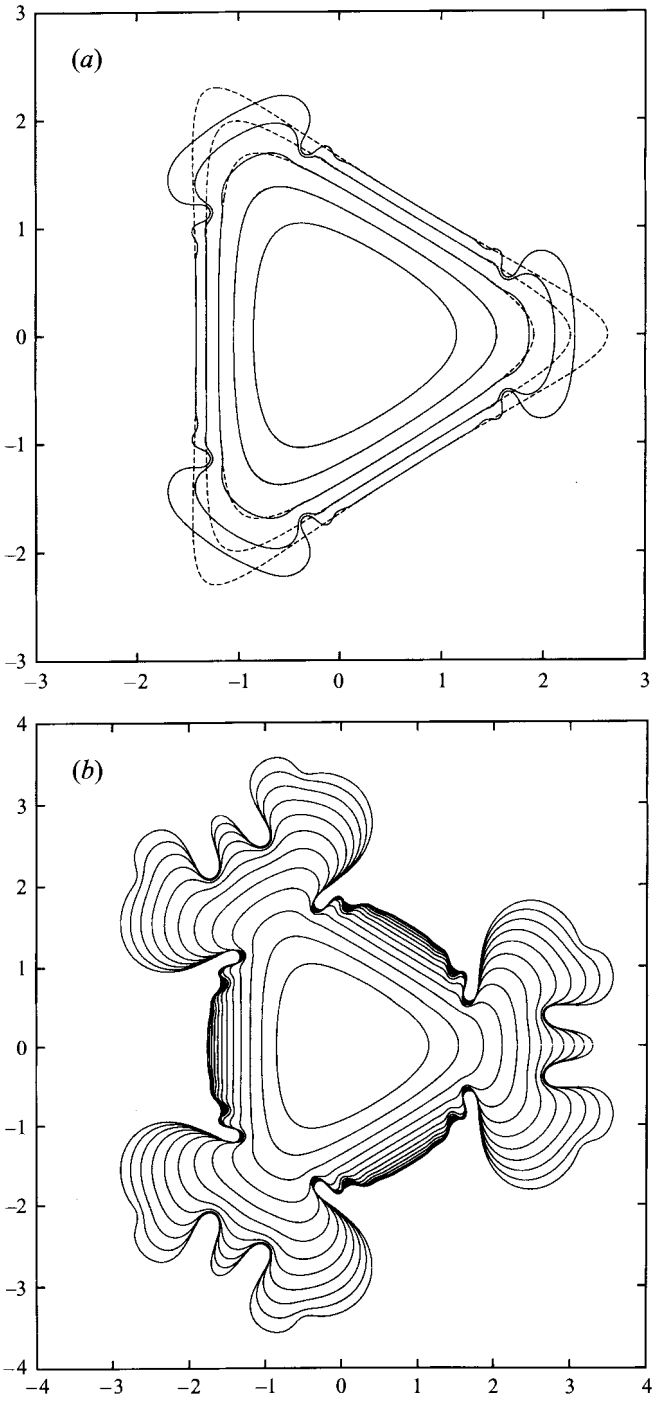

FIGURE 11. (*a*) Evolution of a Hele-Shaw 'bubble' using three-zero initial data of the form (22) with $\zeta_0(0) = 1.5$. We compare the $B = 0.00025$ solution (shown as solid curves) with the exact $B = 0$ solution (22) (dashed curves). In each solution, the time difference between profiles is 0.3. (*b*) Evolution of the $B = 0.00025$ Hele-Shaw bubble in (*a*) over a long time. The time difference between profiles is 0.3 up to $t = 0.9$, after which it is 0.305.

For the kind of initial data currently under consideration, a discretization based on the conformal map parameterization is well suited to resolving the interface. This is clearly the case for the $B = 0$ solution, in which only two non-zero Fourier modes are present in the solution for $t \geqslant 0$ when it is written in the conformal map frame. For small non-zero B this is no longer true; nevertheless, modes $\hat{z}(k)e^{ikv}$ with $k \geqslant 3$ are initially only weakly generated, and at early times in the evolution the conformal map parameterization will require many fewer modes to resolve the interface than one based on an equal-arclength or Lagrangian parameterization.

In our simulations, we solve equation (8) for N equally spaced points on $|\zeta| = 1$ using a pseudospectral method similar to that employed by Dai *et al.* (1991). All derivatives and Hilbert transforms are computed using the discrete Fourier transform. Note that the analyticity of $f(\zeta, t) = z(\zeta, t) + a(t)/\zeta$ for $|\zeta| < 1$ implies that only positive-wavenumber modes such as $\hat{f}(k)e^{ikv}$ with $k > 0$ will be present in the solution. Care must be taken to avoid the spurious generation of modes with negative wavenumber, since these are unstable and quickly grow. We prevent this occurrence by setting modes with negative wavenumber to zero at the end of each time step. A standard fourth-order Adams predictor-corrector method with fixed step size is used to obtain the time update. The threefold symmetry is incorporated into the simulations in order to speed up the calculations. Noise effects are characterized using the same procedures as in the channel case. The filter levels for the 64-bit and 128-bit calculations are also identical to those used earlier. All of the reported calculations correspond to 128-bit runs with a 10^{-25} filter level. As in the channel computations, the number of modes is doubled when the magnitude of the highest k coefficient exceeds the filter level. Unfortunately, owing to the stiffness of the equations of motion and our use of an explicit scheme, the time step typically must be reduced by a factor of 8 when the number of modes is doubled. This limits the feasibility of this method for long-time computations. Nevertheless, the method is sufficient for our purposes here. In a typical run, we begin with $N = 256$ points (discretizing 1/3 of the interface) and a time step of $\Delta t = 0.0005$; each run is stopped when N reaches 2048. As usual, it is checked that reperforming the calculations with a smaller time step does not affect the reported results.

We first consider the onset time for deviations between the $B = 0$ and $B > 0$ solutions for initial data chosen in accordance with (22), with $\zeta_0(0) = 2.0$ and $A(0) = 1.0$. Unless otherwise noted, all of the subsequent computations employ these values. For these initial data, the daughter singularity $\zeta_d(t)$ reaches $|\zeta| = 1$ at $t_d = 1.101$, well before the time $t_c = 15.504$ at which $\zeta_0(t)$ reaches the unit disk in the corresponding zero-surface-tension solution. Thus, at the daughter singularity impact time, the interface is nowhere near cusp formation, and the curvature of the $B = 0$ solution is not large.

The conformal map parameterization utilized in the simulations makes it easy to obtain global comparisons between the $B = 0$ and $B > 0$ solutions. Let $m(t) = \max_v |z_v(v, t) - z_{0v}(v, t)|$ and define t_q as the first time at which $m(t_q) = q$. We again expect that the effects of the daughter singularity cluster will first be felt around the time that its leading edge nears the unit disk, so that the time t_q should vary linearly with $B^{1/3}$ for sufficiently small q and B. Figure 12 plots t_q versus $B^{1/3}$ for $q = 0.0001$, 0.0002, 0.0005, 0.001 and 0.05. The lower curves can be extended to smaller B, since noise effects are less prominent over short times. For small enough q, the marker points exhibit the expected linear behaviour as B tends to zero. Linear extrapolation of the four lower curves to $B = 0$ (using the two leftmost points on each curve) gives limiting values of $t_q(B \to 0) = 1.140 \pm 0.005$, 1.153 ± 0.008, 1.169 ± 0.011,

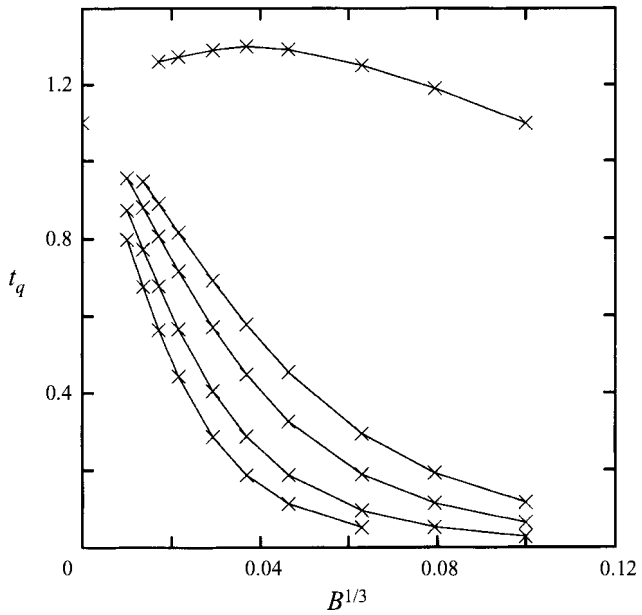

FIGURE 12. The first time t_q at which $\max_v |z_v(v,t) - z_{0v}(v,t)| = q$, plotted versus $B^{1/3}$. Initial data of the form (22) are used, with $\zeta_0(0) = 2.0$. The filter level is set to 10^{-25}. From top to bottom, $q = 0.05$, 0.001, 0.0005, 0.0002, and 0.0001. The theoretical daughter singularity impact time is marked by the half-cross. Linear extrapolation of the four lower curves to $B = 0$ (using the two leftmost points on each curve) leads to limiting values $t_q(B \to 0) = 1.140 \pm 0.005$, 1.153 ± 0.008, 1.169 ± 0.011 and 1.166 ± 0.005 for $q = 0.0001$, 0.0002, 0.0005, and 0.001, respectively (compare with $t_d = 1.101$). The error intervals measure the variation in the $B = 0$ intercepts when the filter level is raised to 10^{-23}.

and 1.166 ± 0.005 for $q = 0.0001$, 0.0002, 0.0005, and 0.001 respectively. These values agree well with the predicted daughter singularity impact time $t_d = 1.101$. The error intervals in the onset times are determined by examining the variation in the plotted quantities when the filter level is increased from 10^{-25} to 10^{-23}. In the problem considered here this procedure provides a reliable estimate of the influence of noise on the computed values. All other error intervals reported in this subsection are generated in a similar fashion.

As in the channel case, the $B^{1/3}$ spatial scale for the singularity cluster is checked by considering a log-log plot of $t_d - t_q$ versus B, for various values of q. This is shown in figure 13. As before, only small values of q are considered. The limiting slope of each curve, computed using the two smallest-B points, is indicated in the figure. These values are near the predicted slope of 1/3, although they are slightly higher. The error bars indicate that, for the values of q considered, the plotted quantities change by a relatively small amount when the filter level is raised to 10^{-23}. This is the case so long as B is greater than approximately 10^{-6}. As B is decreased below 10^{-6}, our simulations show that the differences between the results for the 10^{-23} and 10^{-25} filter levels increase greatly.

A measurement of the extent of the v interval in which z_v differs from z_{0v} should also reveal a linear dependence on $B^{1/3}$, owing to the $O(B^{1/3})$ size of the daughter singularity cluster. Define $s_p(t)$ to be the largest value of $v \in [0, \pi/3]$ for which $|z_v(v,t) - z_{0v}(v,t)| \geqslant p$. Thus, $2s_p(t)$ is the size of the region in which z_v differs from z_{0v}, when v is restricted to one of the three symmetric portions of the interface.

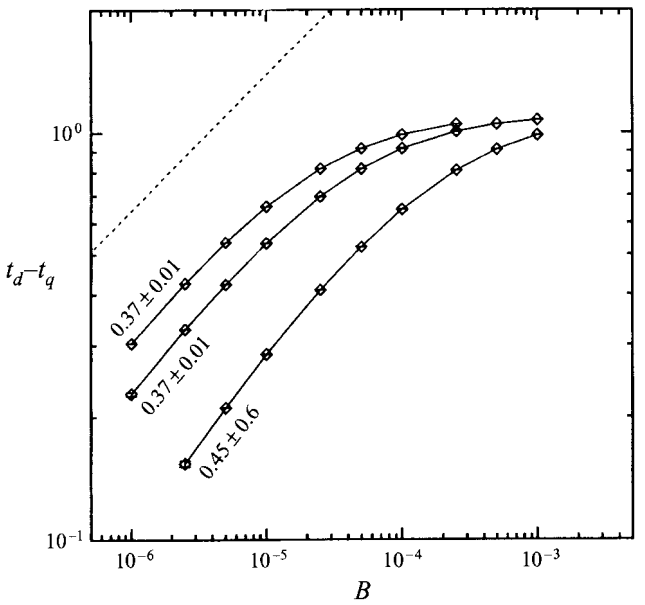

FIGURE 13. Log-log plot of $t_d - t_q$ versus B. The solid curves correspond to (top to bottom) $q = 0.0001$, 0.0002, and 0.001. The dashed line exhibits the theoretically predicted slope of 1/3. Error bars are obtained by comparing results for a filter level of 10^{-25} to those for a level of 10^{-23}. The slope of a line through the last two points on each curve is indicated in the figure, along with an error interval measuring the variation in each slope when the filter level is raised to 10^{-23}.

Figure 14 is a log-log plot of $s_p(t)$ versus B, for several values of p. The plots are obtained at a fixed scaled time $T = -3.4$, where T is defined in (40). This value of T is large enough for $s_p(t)$ to achieve an ample magnitude (for the range of B and p considered), yet small enough so that any advection of the daughter singularity cluster around the unit disk prior to $T = -3.4$ is minimized. Unfortunately, the curves do not exhibit a clear linear behaviour for small B but rather show a bit of unevenness. It is conceivable that the spatial measurement of the daughter singularity cluster is complicated by an internal structure; this possibility is discussed further later in this subsection. Despite this, the *overall* trend of the curves in the figure is more or less consistent with the asymptotic prediction. In particular we see that, on average, the course of the curves follows that of a line with slope 1/3.

It is also possible to examine some of the predicted features of later stages in the evolution, i.e. after the daughter singularity cluster reaches the unit disk and begins to advect around it, possibly causing it to begin to break up (see figure 2*c*). For example, consider the time at which the surface tension term Im ω_v reaches a given $O(1)$ value. The asymptotic theory suggests that this occurs an $O(1)$ time after the daughter singularity time t_d, in the limit $B \to 0$. Let t_r be the time required for $|\text{Im } \omega_v|$ to reach the value r. In figure 15, we show a log-log plot of $t_r - t_d$ versus B for three representative values of r. In order for Im ω_v to reach $O(1)$ in magnitude, the calculations must be performed for relatively long times. The desire to prevent noise effects from becoming prominent at the later times restricts how small B can be taken. Nevertheless, for the smallest values of B and r considered, the slopes of the numerically computed curves appear to be approaching zero, as expected. The asymptotic theory also suggests that the extent of the region over which Im ω_v equals $O(1)$ scales like $O(B^{1/6})$, for fixed time $\tilde{T} = (t - t_d)$ (see the discussion at the end of

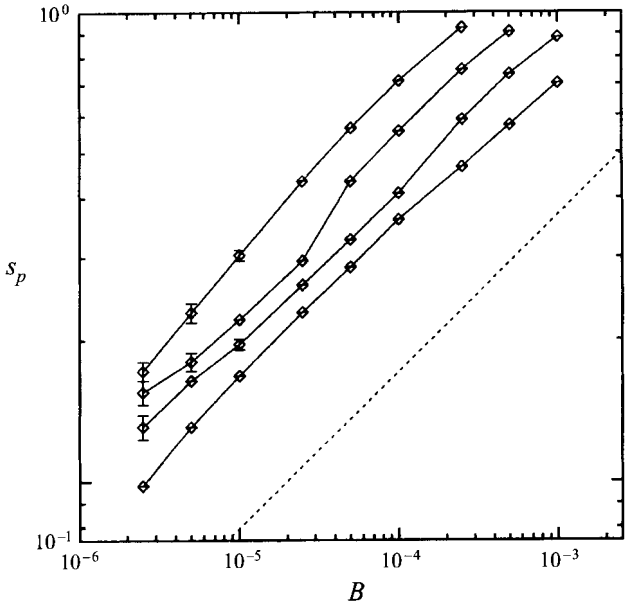

FIGURE 14. Log-log plot of $s_p(t)$ (the extent in v for which $|z_v(v,t) - z_{0v}(v,t)| \geqslant p$) versus B, at fixed scaled time $T = -3.4$. The curves correspond to (top to bottom) $p = 0.00025$, 0.0005, 0.001, and 0.002. Error bars are computed as in figure 13. The dashed lined exhibits the theoretically predicted slope of 1/3.

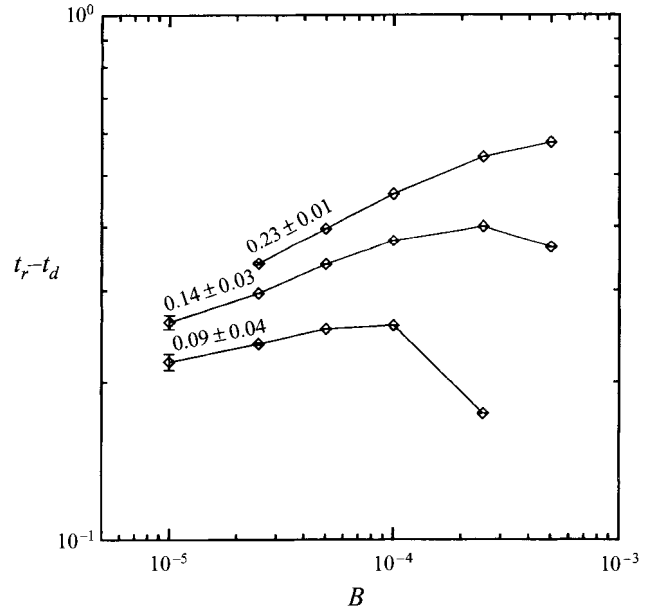

FIGURE 15. Log-log plot of $t_r - t_d$ versus B, where t_r is the time required for the magnitude of the surface tension term Im ω_v to reach the value r. The solid curves correspond to $r = 0.005$ (upper curve), $r = 0.0025$ (middle curve), and $r = 0.001$ (lower curve). The slope of a line through the last two points on each curve is indicated on the figure. The error bars and the error intervals for the slopes are determined as in figure 13.

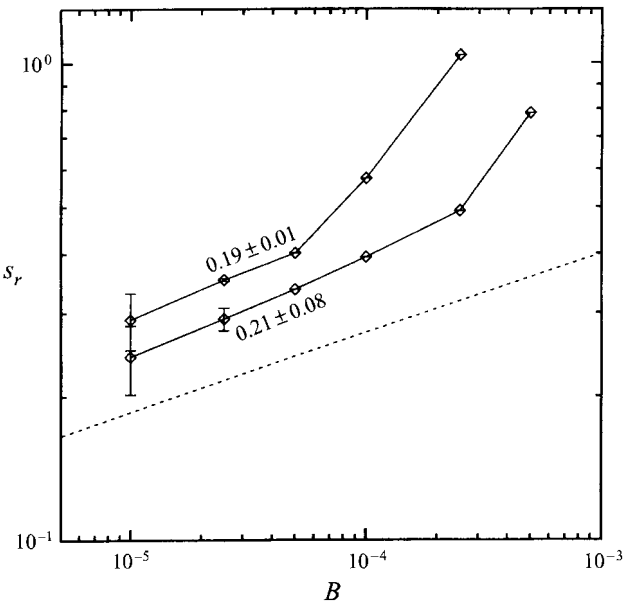

FIGURE 16. Log-log plot of $s_r(t)$ (the extent in v for which $|\text{Im } \omega_v| \geqslant r$) versus B. Each solid curve corresponds to a fixed value of $\tilde{T} = (t - t_d)$ and r. We show results for $\tilde{T} = 0.15$, $r = 0.0001$ (upper curve); and $\tilde{T} = 0.22$, $r = 0.0005$ (lower curve). On each curve, we indicate the slope of a line through the two points with $B = 0.00005$ and $B = 0.000025$. (These points are used instead of two smallest-B points, owing to the potentially large noise induced errors in the $B = 0.00001$ values for the upper two curves). The error bars and the error intervals for the slopes are determined as in figure 13.

§4). Define $s_r(t)$ to be the largest value of $v \in [0, \pi/3]$ for which $|\text{Im } \omega_v| \geqslant r$. A log-log plot of s_r versus B, for various combinations of time $\tilde{T}$ and r, is displayed in figure 16. In each curve, the slope for small B is near $1/6$, which is the predicted behaviour for sufficiently small B and r.

There is some evidence to suggest that the daughter singularity breaks up into several concentrated subclusters as it approaches the unit disk, as diagrammed in figure 2(c). One indication of this behaviour is that ripples which are not due to noise effects are observed to form on the interface, much like those seen near the base of each bulb of air in figure 11(a). If $\kappa(v,t)$ and $\kappa_0(v,t)$ denote the $B > 0$ and $B = 0$ curvatures, respectively, then the extent of the rippling is readily apparent in a plot of $|\kappa - \kappa_0|$ versus $v \in [0, \pi/3]$ (figure 17). The different curves in the plot correspond to $|\kappa - \kappa_0|$ at different times in the evolution. This plot shows that non-zero surface tension introduces localized oscillations in the interface in a region about $v = 0$. We speculate that the oscillations are caused by daughter singularity subclusters which disperse along the interface owing to the action of the separatrix located along the Re $v = 0$ line. One indication of this behaviour is that the function $s_r(t)$ does not smoothly increase as a function of time (see figure 18), but rather exhibits sharp jumps. This suggests that the subclusters which are located closest to $v = 0$ are the first to 'impinge' upon the unit disk and influence the physical interface, followed later by the subclusters which are the next nearest to $v = 0$, and so on. Such a scenario is sketched in figure 2(c). It is expected that the size of the subclusters will decrease with B. This expectation is consistent with the data in figure 18, which show that the

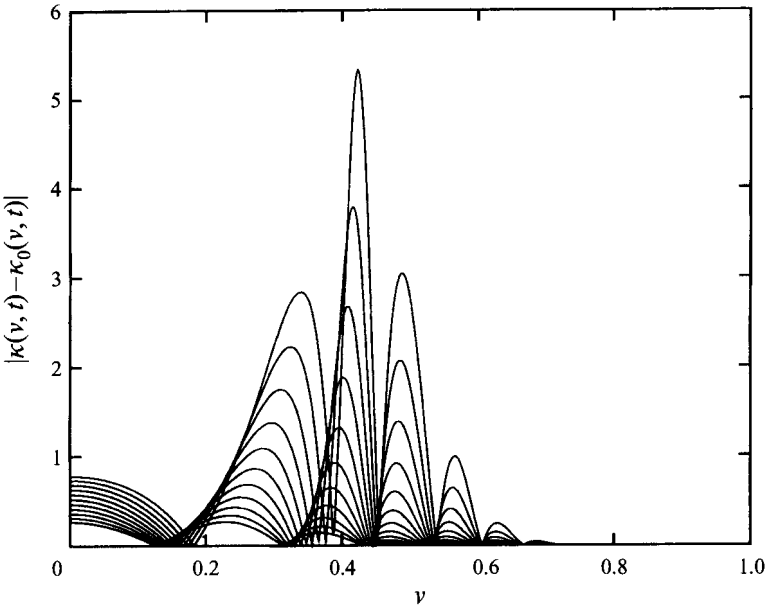

FIGURE 17. Plot of $|\kappa - \kappa_0|$ versus v, for $t = 1.25$ to 1.75 in steps of 0.05. We set $B = 0.0001$. The range of v corresponds to one-half of one of the three symmetric portions of the interface.

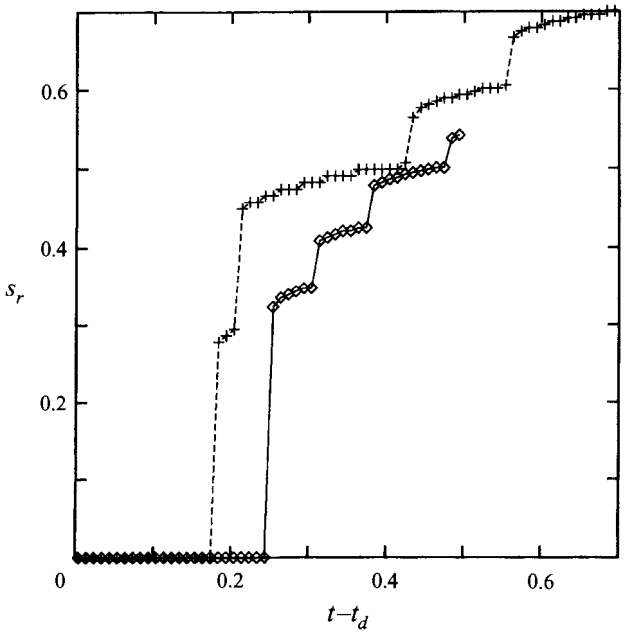

FIGURE 18. Plot of $s_r(t)$ versus $t - t_d$, for $r = 0.001$. Surface tension values are $B = 0.00025$ (+) and $B = 0.00005$ ($\diamond$)

jumps in $s_r(t)$ occur more frequently and are smaller in magnitude for the smaller values of B.

Finally, we remark that we have also computed the effects of small surface tension on a second family of exact solutions in the radial geometry, namely one that contains

three symmetrically located zeros (as in (22)) plus three symmetrically placed poles. Earlier, Dai & Shelley (1994) had numerically investigated small-surface-tension effects for a specific initial condition of this type, in which the zeros are radially aligned with the poles but are further from the origin. In this case, asymptotic theory suggests that the daughter singularities will not impinge upon $|\zeta| = 1$ in $O(1)$ time, which is consistent with their observations. On the other hand, when the angular positions of the zeros and poles are staggered, we observed daughter singularity effects at the time t_d, as predicted by the asymptotics. However, the overall effect on the shape was much smaller than for the case of three zeros alone.

6. Conclusions

Numerical evidence has been presented to show that a smoothly evolving zero-surface-tension solution of the Hele-Shaw equations can be singularly perturbed by the presence of arbitrarily small non-zero surface tension in order-one time. The numerics support the essential features of an asymptotic theory originally introduced by Tanveer (1993) and extended here. The behaviour is explained by the presence of localized clusters of singularities (daughter singularities) which are born at each point in the complex domain where $z_{0\zeta}(\zeta, t) = 0$. To leading order in B, and for $t = O(1)$, each singularity in the daughter singularity cluster moves according to (20), i.e. it moves as if it were a singularity of the zero-surface-tension solution $z_0(\zeta, t)$. Thus, the daughter singularity approaches the physical domain in a manner which can be predicted from knowing the corresponding zero-surface-tension solution. Once the daughter singularity approaches $|\zeta| = 1$, the cluster breaks up and advects towards the points of symmetry ($\zeta = \pm 1$ in the channel case, for instance).

The numerical simulations show that the daughter singularity clusters cause large interfacial deformations when they come to within an $O(B^{1/3})$ neighbourhood of the unit disk. In this case, the calculations show good agreement with analytically predicted scalings. Other situations are found in which the motion of the daughter singularity cluster toward the physical domain is impeded by the presence of other singularities. When this happens, there is no significant difference between the $B = 0$ and $0 < B \ll 1$ solutions in $O(1)$ time.

Our results are particularly interesting for the case of steady finger motion in a channel, where the zero-surface-tension equations allow a continuum of steady finger solutions of arbitrary finger width. On the other hand, experiments and numerical simulations for small surface tension show a unique steady finger solution of a given (surface-tension-dependent) width. Our computations show that the daughter singularity produces a transition from an arbitrary finger solution to one with the selected steady width in $O(1)$ time for $B \ll 1$. Furthermore, given the analytically extended initial data, the onset time of the transition can be easily predicted. However, we point out that although the numerical calculations in the physical domain support the essential features of the asymptotic theory, such as the creation of a daughter singularity and its advection towards the real domain, they are unable to determine if the scenario described in stages (ii)–(iv) of §4 is accurate. Indeed, in the scalings that have been verified here, only the relation (39) is crucial; it is conceivable that other dynamics at $t = O(B^{2/7})$ can also lead to (39).

The authors would like to acknowledge support from NASA grant NAG 3-1415 and NSF grant DMS 9500986 (S.T.), Department of Energy contract DE-FG02-

92ER14270 (M.S. and S.T.), and an NSF Postdoctoral Fellowship (M.S.). We also acknowledge the computing resources received from the Ohio Supercomputer Center.

REFERENCES

ARNEODO, A., COUDER, Y., GRASSEAU, G., HAKIM, V. & RABAUD, M. 1989 Uncovering the analytical Saffman-Taylor finger in unstable viscous fingering and diffusion limited aggregation. *Phys. Rev. Lett.* **63**, 984.

BAKER, G., SIEGEL, M. & TANVEER, S. 1995 A well-posed numerical method to track isolated conformal map singularites in Hele-Shaw flow. *J. Comput. Phys.* **120**, 348.

BENSIMON, D. 1986 Stability of viscous fingering. *Phys. Rev.* A **33**, 1302.

BENSIMON, D., KADANOFF, L.P., LIANG, S., SHRAIMAN, B.I., & TANG, C. 1986 Viscous flows in two dimensions. *Rev. Mod. Phys.*, **58**, 977.

COMBESCOT, R., DOMBRE, T., HAKIM, V., POMEAU, Y. & PUMIR, A. 1986 Shape selection for Saffman-Taylor fingers, *Phys. Rev. Lett.* **56**, 2036.

COMBESCOT, R., DOMBRE, T., HAKIM, V., POMEAU, Y. & PUMIR, A. 1987 Analytic theory of the Saffman-Taylor fingers, *Phys. Rev.* A **37**, 1270.

CONSTANTIN, P. & PUGH, M. 1993 Global solutions for small data to the Hele-Shaw problem. *Nonlinearity* **6**, 393.

DAI, W., KADANOFF, L.P & ZHOU, S. 1991 Interface dynamics and the motion of complex singularities. *Phys. Rev.* A **43**, 6672.

DAI, W. & SHELLEY, M. 1994 A numerical study of the effect of surface tension and noise on an expanding Hele-Shaw bubble. *Phys. Fluids* A **5**, 2131.

DEGREGORIA, A. J. & SCHWARTZ, L. W. 1985 Finger breakup in Hele-Shaw cells. *Phys. Fluids* **28**, 2313.

DEGREGORIA, A. J. & SCHWARTZ, L. W. 1986 A boundary-integral method for two-phase displacement in Hele-Shaw cells. *J. Fluid Mech.* **164**, 383.

DORSEY, A. & MARTIN, O. 1987 Saffman-Taylor fingers with anisotropic surface tension. *Phys. Rev.* A **35**, 3989.

DUCHON, J. & ROBERT, R. 1984 Evolution d'une interface par capillarité et diffusion de volume. *Ann. Inst. H. Poincaré* **1**, 361.

GALIN, L. A. 1945 *Dokl. Akad. Nauk. SSSR* **47**, 246 (in Russian).

HOMSY, G. 1987 Viscous fingering in porous media. *Ann. Rev. Fluid Mech.* **19**, 271.

HONG, D. & LANGER, J. 1986 Analytic theory for the selection of Saffman-Taylor fingers. *Phys. Rev. Lett.* **56**, 2032.

HOU, T., LOWENGRUB, J. & SHELLEY, M. 1994 Removing the stiffness from interfacial flows with surface tension. *J. Comput. Phys.* **114**, 312.

HOWISON, S. D. 1985 Bubble growth in porous media and Hele-Shaw cells. *Proc. R. Soc. Edin.* A **102**, 141.

HOWISON, S. D. 1986 Fingering in Hele-Shaw cells. *J. Fluid Mech.* **167**, 439.

HOWISON, S. D. 1986 Cusp development in Hele-Shaw flow with a free surface. *SIAM J. Appl. Math* **46**, 20.

HOWISON, S. D. 1991 Complex variable methods in Hele-Shaw moving boundary problems. *Eur. J. Appl. Maths* **3**, 209.

KESSLER, D., KOPLIK, J. & LEVINE, H. 1988 Pattern selection in fingered growth phenomena. *Adv. Phys.* **37**, 255.

KRASNY, R. 1986 A study of singularity formation in a vortex sheet by the point-vortex approximation. *J. Fluid Mech.* **167**, 65.

KUNKA M., FOSTER, M. R., & TANVEER, S. 1996 In preparation.

LACEY, A. A. 1982 Moving boundary problems in the flow of liquid through porous media. *J. Austral. Math. Soc.* **B24**, 171.

MAXWORTHY, T. 1987 The nonlinear growth of a gravitationally unstable interface in a Hele-Shaw cell. *J. Fluid Mech.* **177**, 207.

MCLEAN, J. W. & SAFFMAN, P. G. 1981 The effect of surface tension on the shape of fingers in a Hele-Shaw cell. *J. Fluid Mech.* **102**, 455.

MEIBURG, E., & HOMSY, G. M. 1988 Nonlinear unstable viscous fingers in Hele-Shaw flows. II. Numerical simulation. *Phys. Fluids* **31**, 429.

PARK, C. W. & HOMSY, G. M. 1985 Two-phase displacement in Hele-Shaw cells: theory. *J. Fluid Mech.* **139**, 291.

PELCE, P. 1988 *Dynamics of Curved Fronts.* Academic.

POLUBARINOVA-KOCHINA, P. 1945 *Dokl. Akad. Nauk. SSSR* **47**, 254 (in Russian).

REINELT, D. A. 1987 Interface conditions for two-phase displacement in Hele-Shaw cells. *J. Fluid Mech* **183**, 219.

REINELT, D. A. 1987 The effect of thin film variations and transverse curvature on the shape of fingers in a Hele-Shaw cell. *Phys. Fluids* **30**, 2617.

RICHARDSON, S. 1972 Hele-Shaw flows with a free boundary produced by the injection of fluid into a narrow channel. *J. Fluid Mech.* **56**, 609.

SAFFMAN, P. G. 1959 Exact solution for the growth of fingers from a flat interface between two fluids. *Q. J. Mech. Appl. Maths* **12,** 146.

SAFFMAN, P. G. 1986 Viscous fingering in a Hele-Shaw cell. *J. Fluid Mech.* **173**, 73.

SAFFMAN, P. G. & TAYLOR, G. I. 1958 The penetration of a fluid into a porous medium of Hele-Shaw cell containing a more viscous fluid. *Proc. R. Soc. Lond.* A **245**, 312.

SARKAR, S. & JASNOW, D. 1987 Quantitative test of solvability theory for the Saffman-Taylor problem. *Phys. Rev.* A **35**, 4900.

SCHWARTZ, L. & DEGREGORIA, A. 1987 Simulation of Hele-Shaw fingering with finite capillary number effects included. *Phys. Rev.* A **35**, 276.

SHRAIMAN, B. I. 1986 On velocity selection and the Saffman-Taylor problem. *Phys. Rev. Lett.* **56,** 2032.

SHRAIMAN, B. I. & BENSIMON, D. 1985 Singularities in nonlocal dynamics. *Phys. Rev.* A **30,** 2840.

SIEGEL, M. & TANVEER, S. 1996 Singular perturbation of smoothly evolving Hele-Shaw solutions. *Phys. Rev. Lett.* **56,** 419.

TANVEER, S. 1987 Analytic theory for the linear stability of Saffman-Taylor finger. *Phys. Fluids* **30,** 2318.

TANVEER, S. 1990 Analytic theory for the selection of Saffman-Taylor finger in the presence of thin-film effects. *Proc. R. Soc. Lond.* A **428,** 511.

TANVEER, S. 1991 Viscous displacement in a Hele-Shaw cell, In *Asymptotics Beyond All Orders* (ed. H. Segur, S. Tanveer & H. Levine) p. 131. Plenum.

TANVEER, S. 1993 Evolution of a Hele-Shaw interface for small surface tension. *Phil. Trans. R. Soc. Lond.* A **343,** 1 (see also erratum 1994).

TANVEER, S. 1995 Asymptotic calculation of thin-film effects on Hele-Shaw fingering. *J. Fluid Mech.* (submitted).

TRYGGVASSON, G. & AREF, H. 1983 Numerical experiments on Hele-Shaw flow with a sharp interface. *J. Fluid Mech.* **136**, 1.

TRYGGVASON, G. & AREF, H. 1985 Finger-interaction mechanisms in stratified Hele-Shaw flow. *J. Fluid Mech.* **154,** 287.

ZHURAVLEV, P. 1956 *Zap Leningrad Com. Inst.* **133,** 54 (in Russian).